Malaysian Journal of Mathematical Sciences 17(3): 379–412 (2023)
https://doi.org/10.47836/mjms.17.3.09

Malaysian Journal of Mathematical Sciences

Journal homepage: https://mjms.upm.edu.my

# Dynamical Discussion and Diverse Soliton Solutions via Complete Discrimination System Approach Along with Bifurcation Analysis for the Third Order NLSE

Rizvi, S. T. R.[1], Seadawy, A. R.*[2], and Mustafa, B.[1]

[1]*Department of Mathematics, COMSATS University Islamabad, Lahore Campus, Pakistan*
[2]*Mathematics Department, Faculty of Science, Taibah University, Al-Madinah Al-Munawarah, 41411, Kingdom of Saudi Arabia*

*E-mail: aabdelalim@taibahu.edu.sa*
**Corresponding author*

*Received: 10 July 2023*
*Accepted: 2 August 2023*

## Abstract

The purpose of this study is to introduce the wave structures and dynamical features of the third-order nonlinear Schrödinger equations (TONLSE). We take the original equation and, using the traveling wave transformation, convert it into the appropriate traveling wave system, from which we create a conserved quantity known as the Hamiltonian. The Jacobian elliptic function solution (JEF), the hyperbolic function solution, and the trigonometric function solution are just a few of the optical soliton solutions to the equation that may be found using the complete discrimination system (CDS) of polynomial method (CDSPM) and also transfer the JEF into solitary wave (SW) soltions. It also includes certain dynamic results, such as bifurcation points and critical conditions for solutions, that might be utilized to explore the dynamic features of the equation employing the CDSPM. This method could also be used for qualitative analysis. The qualitative analysis is used to illustrate the equilibrium points and phase potraits of the equation. Phase portraits are visual representations used in dynamical systems to illustrate a system's behaviour through time. They can provide crucial information about a system's stability, periodic behaviour, and the presence of attractors or repellents.

**Keywords:** TONLSE; qualitative analysis; CDSPM; bifurcation method.

# 1 Introduction

Soliton is a type of ultrashort pulse that is also known as a SW. It was initially proposed while researching fluid physics [33, 21]. Solitons have been discovered in recent years as a result of extensive study by mathematicians and physicists [21, 32]. Solitons include acoustic solitons, electrical solitons, and optical solitons [16, 5]. In general, SW are created by solving a nonlinear partial differential equation, which may be thought of as both a nonlinear behavior of matter and a solution of nonlinear partial differential equations [8]. Loss and dispersion are the two most significant issues in optical fiber transmission. Dispersion broadens the optical pulse and distorts the signal [7]. Simultaneously, the nonlinear nature of fiber optics causes the pulse to become narrow owing to the compression effect [23]. Optical solitons offer the benefits of high transmission capacity, low bit error rate, high fidelity, and long-distance transmission by striking a balance between the two types of optical fiber effect [3, 29]. In recent years, researchers have employed the NLSE to characterize the propagation of optical solitons in various medium conditions [22, 2]. Because optical soliton provides an NLSE solution [28, 36], it is critical to obtain its exact solutions [1, 6]. There are various ways for studying, analyzing, and solving NLSE [19, 27], including the Hirota bilinear approach [25], inverse scaling transformation [4], homogeneous balancing scheme [14], Darboux transformation method [18], function expansion approach [24] and many other methods. However, the optical solitons generated by various methods offer distinct benefits and disadvantages in their characteristics.

Our aim to study the TONLSE in order to introduce the wave structure and the variety of optical soliton by using CDSPM [9]. Liu introduced a CDSPM to classify single traveling wave solutions to nonlinear equations, which resulted in several beneficial outcomes [35, 10]. The CDSPM's core principle is to convert the original equation into an integral form, then analysing the connection between the roots and coefficients to identify the travelling wave solutions [11, 12]. It may be used to identify critical points where bifurcations occur, as well as to classify the various kinds of bifurcations that may occur at each critical point. Bifurcations can happen when the stability of an equilibrium point or periodic solution varies as a parameter is changed. It can result in the creation of new types of solutions or the disappearance of existing ones. The bifurcation approach, which is used to examine the behaviour of dynamical systems when parameters are altered, includes qualitative analysis [17]. The qualitative analysis includes analyzing the qualitative aspects of the system, such as the number and stability of fixed points, periodic orbits, and their bifurcations [30, 20]. Researchers can get insight into the system's long-term behaviour by finding the bifurcation points and their related bifurcation diagrams [34, 26]. Consequently, the purpose of this article is to illustrate that the CDSPM may be used to examine the dynamic features of the TONLSE [13, 31]. Moreover, we give numerous dynamic results, such as critical conditions and bifurcation points for the solutions, to support this argument.

The paper is structured as follows: Section 2 offers the mathematical analysis of our governing model, while Section 3 applies the use CDS to fourth-orderÂ polynomials. Section 4 employs the use of CDS for third-orderÂ polynomials, while Section 5 caries out the SW solutions. Finally, in Section 6 provides a full description of our findings and in Section 7, we present a summary of our findings.

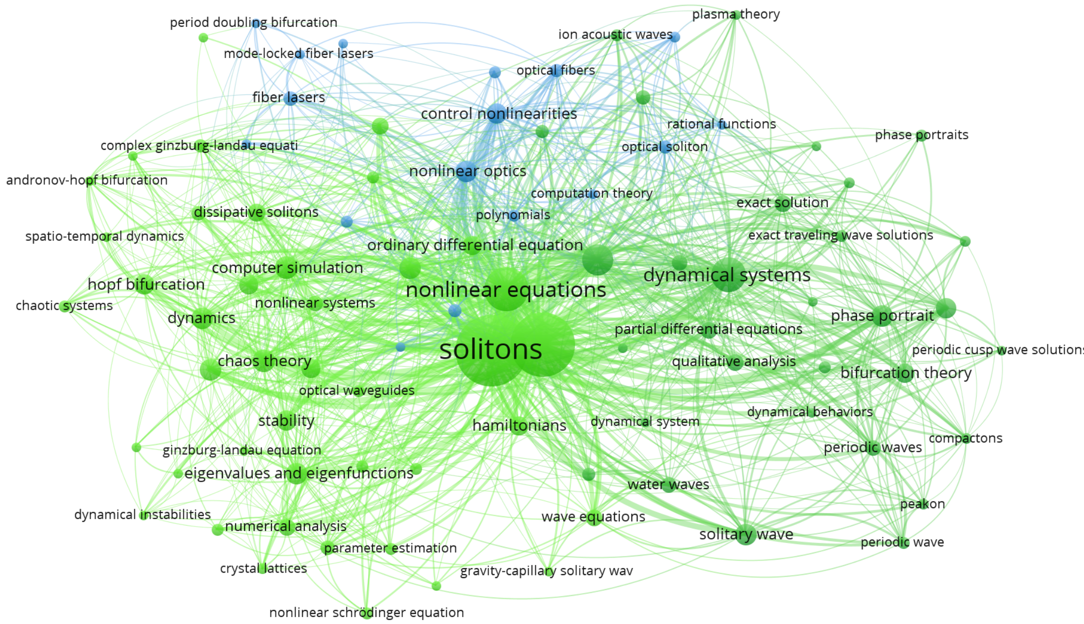


Figure 1: Bibliometric networks for bifurcation and soliton.

## 2 Mathematical Model

In this paper, we investigate the TONLSE with third order linear and nonlinear dispersion [30, 20]:

$$i\varpi_x + \varsigma_1\Big(\varpi_{tt} + 2|\,\varpi\,|^2\varpi\Big) - i\varsigma_2\Big(\varpi_{ttt} + 6|\,\varpi\,|^2\varpi_t\Big) = 0, \tag{1}$$

where $\varpi(x,t)$ represents the soliton envelope amplitude, $\varsigma_1$ is the coefficient of group velocity dispersion, and $\varsigma_2$ is the third-order dispersion effect. The above equation produces solutions that are extremely useful in the study of nonlinear phenomena in many fields of science and engineering, including plasma physics, optical engineering, fluid dynamics, oceanography engineering, nonlinear dynamics, condensed-matter physics, and many others. We assume the following transformation [26]:

$$\varpi(x,t) = \Lambda(\mu)\exp^{[i\Psi(x,t)]}, \tag{2}$$

where,

$$\Psi(x,t) = -\kappa t + \psi x + p, \qquad \mu = t - \omega x. \tag{3}$$

In terms of its real and imaginary parts, equation (1) may be expressed as follows:

$$\Big(\varsigma_1 - 3\kappa\varsigma_2\Big)\Lambda'' + \Big(\varsigma_2\kappa^3 - \varsigma_1\kappa^2 - \psi\Big)\Lambda + \Big(2\varsigma_1 - 6\varsigma_2\kappa\Big)\Lambda^3 = 0, \tag{4}$$

and

$$-\varsigma_2\Lambda''' - 6\varsigma_2\Lambda^2\Lambda' + \Big(3\varsigma_2\kappa^2 - \omega - 2\varsigma_1\kappa\Big)\Lambda' = 0. \tag{5}$$

Equation (4) and equation (5) can be substituted to yield the following constraint conditions

$$\omega = 3\varsigma_2\kappa^2 - 2\varsigma_1\kappa. \tag{6}$$

Now, dividing both sides of equation (4) by $\varsigma_1 - 3\kappa\varsigma_2$ yields

$$\Lambda'' + \frac{\varsigma_2\kappa^3 - \varsigma_1\kappa^2 - \psi}{\varsigma_1 - 3\kappa\varsigma_2}\Lambda + \frac{2\varsigma_1 - 6\varsigma_2\kappa}{\varsigma_1 - 3\kappa\varsigma_2}\Lambda^3 = 0. \tag{7}$$

Let, $E = \dfrac{\varsigma_2\kappa^3 - \varsigma_1\kappa^2 - \psi}{\varsigma_1 - 3\kappa\varsigma_2}$ and $F = \dfrac{2\varsigma_1 - 6\varsigma_2\kappa}{\varsigma_1 - 3\kappa\varsigma_2}$, then, the equation (7) becomes,

$$\Lambda'' + E\Lambda + F\Lambda^3 = 0. \tag{8}$$

Since, multiply equation (8) with $2\Lambda' d\mu$ and integration yield,

$$(\Lambda')^2 + E\Lambda^2 + \frac{F}{2}\Lambda^4 + 2C = 0, \tag{9}$$

where $C$ is the constant of integration.

## 3 Application of CDS for Fourth Degree Polynomial

So, equation (9) becomes,

$$(\Lambda')^2 = \frac{-F}{2}\Big(\Lambda^4 + o_2\Lambda^2 + o_1\Lambda + o_0\Big), \tag{10}$$

where,

$$o_2 = \frac{2E}{F}, \qquad o_1 = 0, \qquad o_0 = \frac{4C}{F}. \tag{11}$$

We just take into account the $F < 0$ situation in equation (10), and the $F > 0$ case may be treated in a manner equivalent to that. Equation (10)'s integral form is

$$\int \frac{d\Lambda}{\sqrt{\Lambda^4 + o_2\Lambda^2 + o_1\Lambda + o_0}} = \pm\sqrt{\frac{-F}{2}}(\mu - \mu_0), \tag{12}$$

where $\mu_0$ is an integral constant. Now, denote $F(\Lambda) = \Lambda^4 + o_2\Lambda^2 + o_1\Lambda + o_0$ and CDS as follows,

$$\begin{gathered} D_1 = 4, \qquad D_2 = -o_2, \qquad D_3 = -2o_2^3 + 8o_2o_0 - 9o_1^2, \\ D_4 = -o_2^3o_1^2 + 4o_2^2o_0 + 36o_2o_1^2o_0 - 32o_2^2o_0 - \frac{-27}{4}o_1^4 + 63o_0^3, \qquad E_2 = 9o_2^2 - 32o_2o_0. \end{gathered} \tag{13}$$

The dynamic system shown below may be seen to be equal to equation (11),

$$\begin{cases} \Lambda' = \zeta(\lambda), \\ \zeta' = -\dfrac{F}{2}\Big(4\Lambda^3 + 2o_2\Lambda + o_1\Big). \end{cases} \tag{14}$$

The following is the Hamiltonian for the system,

$$H(\Lambda, \zeta) = \frac{\zeta^2}{2} + \frac{F}{4}(\Lambda^4 + o_2\Lambda^2 + o_1\Lambda + o_0). \tag{15}$$

Therefore, the potential energy may be written as,

$$U(\Lambda) = \frac{F}{4}\Big(\Lambda^4 + o_2\Lambda^2 + o_1\Lambda + o_0\Big). \tag{16}$$

### 3.1 Qualitative analysis

It is required to determine the roots of $U'(\Lambda)$ in order to analyze the dynamic aspects of equation (12), [17],

$$U'(\Lambda) = -F\Big(\Lambda^3 + j_1\Lambda + j_0\Big), \tag{17}$$

where $j_1 = \frac{o_2}{2}$ and $j_0 = \frac{o_1}{4}$, whose CDS is given by

$$\Delta = -\left(\frac{j_0^2}{4} + \frac{j_1^3}{27}\right). \tag{18}$$

Three situations must be explored utilizing the CDSPM in accordance with the form of $U'(\Lambda)$.

**Case 1:** $\Delta = 0 \;\;\&\;\; j_1 = 0$,

$$U'(\Lambda) = -F\Lambda^3. \tag{19}$$

The cuspidal point, $(0, 0)$, is the only equilibrium point for the dynamic system. Figure 2 shows the global phase portraits for these circumstances when $F = \pm 1$.

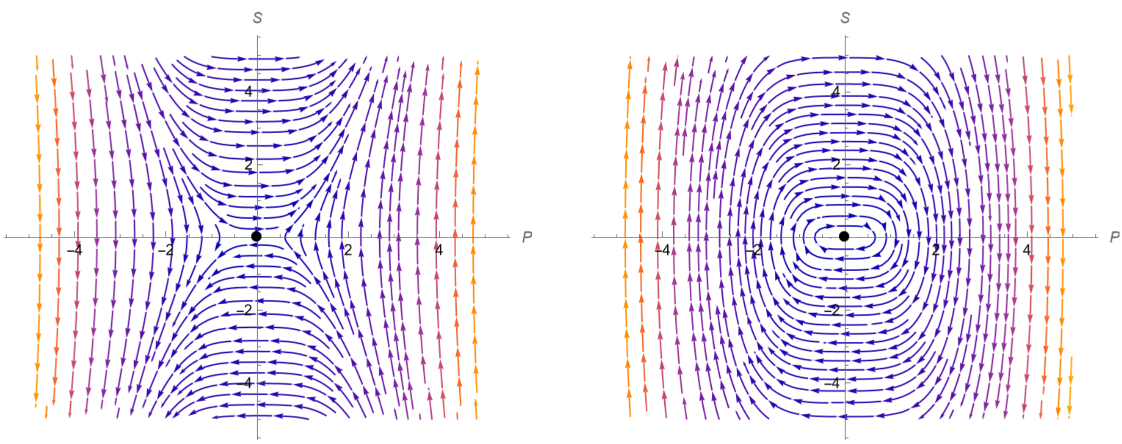


Figure 2: In Case 1, the behavior of the System 14 described over time can be observed through its corresponding phase portraits: (a) $F = 1$, (b) $F = -1$.

**Case 2:** $\Delta > 0 \;\;\&\;\; j_1 < 0$,

$$U'(\Lambda) = -F(\Lambda - p)(\Lambda - q)(\Lambda - q), (p + q + r = 0). \tag{20}$$

where $p > q > r$. In the dynamic system, there are three equilibrium points: $(p, 0)$, $(q, 0)$, and $(r, 0)$. $(p, 0)$ and $(q, 0)$ are saddle points, whereas $(r, 0)$ is a centre. For instance, when $j_1 = -9$, $j_0 = 0$, $p = 3$, $q = 0$ and $r = -3$ are present. The global phase portraits for $F = \pm 1$ are shown in Figure 3.

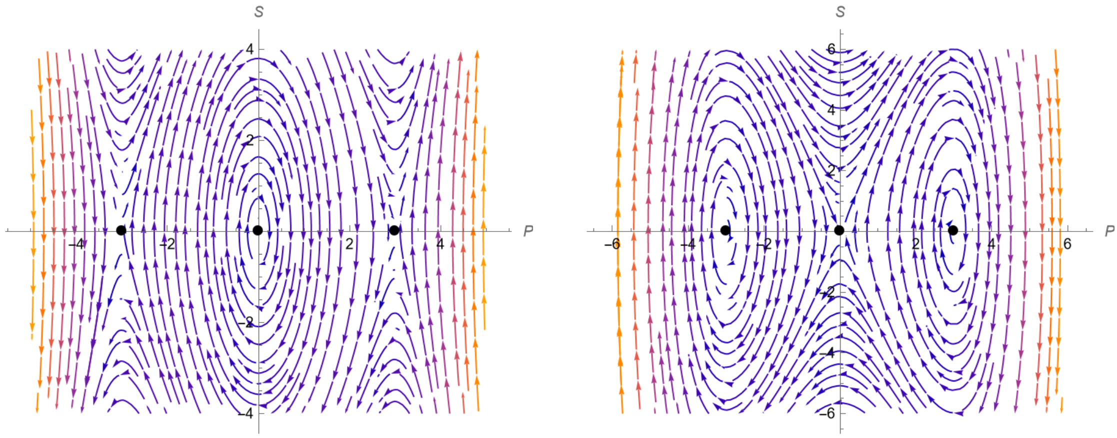


Figure 3: In Case 2, the behavior of the System 14 over time can be observed through its phase portraits: (a) $F = 1$, (b) $F = -1$.

**Case 3:** $\Delta < 0$,

$$U'(\Lambda) = -F(\Lambda - u)[(\Lambda - v)^2 + h^2], (u + 2v = 0). \tag{21}$$

There is an equilibrium point in the dynamic system at $(0, 0)$. The equivalent global phase portraits may be observed in Figure 4 when $j_0 = 0$, $j_1 = 1$ and $F = \pm 1$.

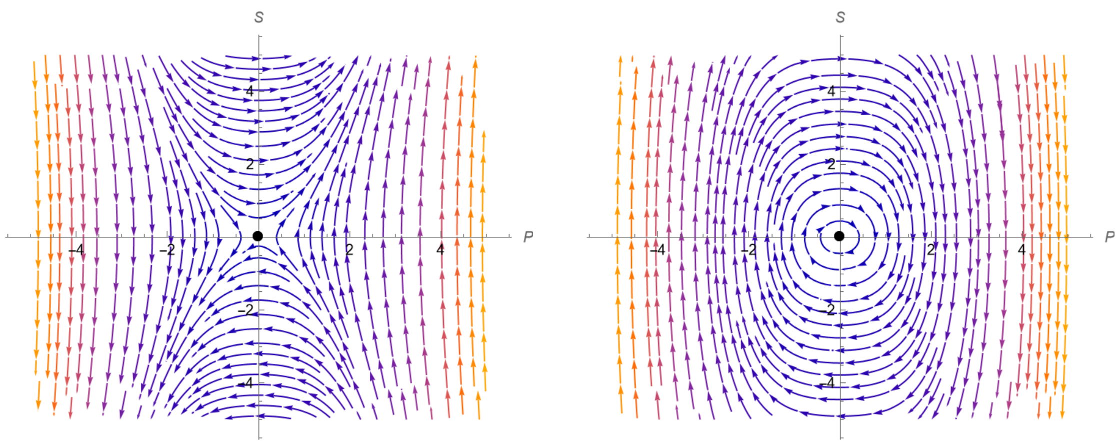


Figure 4: In Case 3, the behavior of the System 14 over time is depicted by its phase portraits: (a) $F = 1$, (b) $F = -1$.

The findings aboveÂ imply that the modification of parameters, particularly the equilibrium points, significantly influencesÂ the dynamic characteristics. The type of equilibrium points and bifurcation may be easily analyzed using CDSPM.

### 3.2 Exact solutions

The preceding studies led to the conclusion that periodic and soliton solutions exist. Our next goal is to use CDSPM to get the exact answer. Below is a list of each and every solution.

**Case 1:** $D_2 < 0$, $D_3 = 0$, and $D_4 = 0$. Then we have

$$F(\Lambda) = ((\Lambda - \pi)^2 + \rho)^2. \tag{22}$$

Putting the equation (22) into equation (12), thus we have

$$\Lambda = \pi + \rho \tan\left(\rho\sqrt{\frac{-F}{2}}(\mu - \mu_0)\right). \tag{23}$$

Therefore, we find the solution

$$\varpi(x,t) = \pi + \rho \tan\left(\rho\sqrt{\frac{-F}{2}}(\mu - \mu_0)\right) \exp^{\left[i\left(-\kappa t + \psi x + p\right)\right]}, \tag{24}$$

which is a periodic solution.

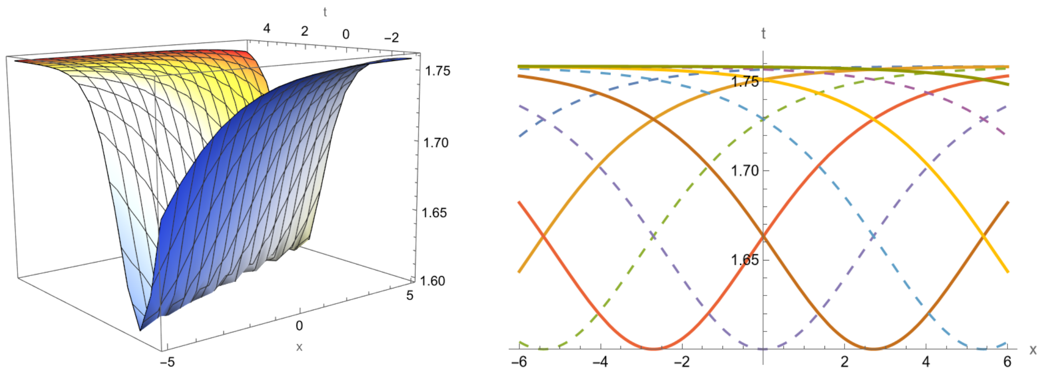


Figure 5: The visual representation of $\varpi(x,t)$ described in equation (24) can be obtained by setting $\pi = 1.6$, $\rho = 0.73$, $\varsigma_1 = 1.52$, $\varsigma_2 = 2.25$, $\psi = 0.65$, $\mu_0 = 0$, $p = 0$, and $\kappa = 0.55$.

**Case 2:** $D_2 = 0$, $D_3 = 0$, and $D_4 = 0$. Thus, we have

$$F(\Lambda) = \Lambda^4. \tag{25}$$

Hence, we have

$$\Lambda = -\sqrt{\frac{-2}{F}}(\mu - \mu_0)^{-1}. \tag{26}$$

Furthermore, we get the solution

$$\varpi(x,t) = -\sqrt{\frac{-2}{F}}(\mu - \mu_0)^{-1} \exp^{\left[i\left(-\kappa t + \psi x + p\right)\right]}, \tag{27}$$

which is a rational solution.

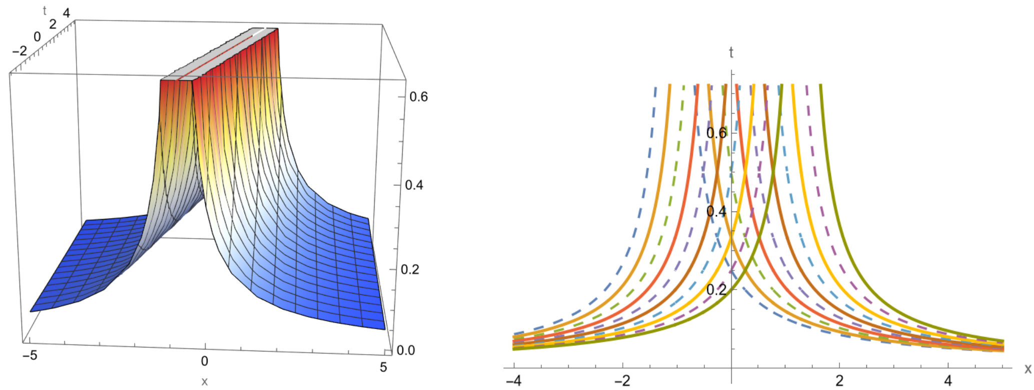


Figure 6: The visual display of $\varpi(x,t)$ described in equation (27) can be obtained by setting $\varsigma_1 = 1.52$, $\varsigma_2 = 1.25$, $\psi = 0.65$, $\mu_0 = 0$, $p = 0$, and $\kappa = 1.5$.

**Case 3:** $D_2 > 0$, $D_3 = 0$, $D_4 = 0$, and $E_2 > 0$. Thus, we have

$$F(\Lambda) = (\Lambda - \Xi)^2(\Lambda - \Gamma)^2. \tag{28}$$

Hence, we have

$$\Lambda = \frac{\Gamma - \Xi}{2}\left(\coth \frac{(\Xi - \Gamma)\sqrt{\frac{-F}{2}}(\mu - \mu_0)}{2} - 1\right) + \Gamma, \tag{29}$$

$$\Lambda = \frac{\Gamma - \Xi}{2}\left(\tanh \frac{(\Xi - \Gamma)\sqrt{\frac{-F}{2}}(\mu - \mu_0)}{2} - 1\right) + \Gamma. \tag{30}$$

Furthermore, we get the two solutions

$$\varpi(x,t) = \left(\frac{\Gamma - \Xi}{2}\left(\coth \frac{(\Xi - \Gamma)\sqrt{\frac{-F}{2}}(\mu - \mu_0)}{2} - 1\right) + \Gamma\right)\exp^{\left[i\left(-\kappa t + \psi x + p\right)\right]}, \tag{31}$$

$$\varpi(x,t) = \left(\frac{\Gamma - \Xi}{2}\left(\tanh \frac{(\Xi - \Gamma)\sqrt{\frac{-F}{2}}(\mu - \mu_0)}{2} - 1\right) + \Gamma\right)\exp^{\left[i\left(-\kappa t + \psi x + p\right)\right]}, \tag{32}$$

which are a solitary wave solutions.

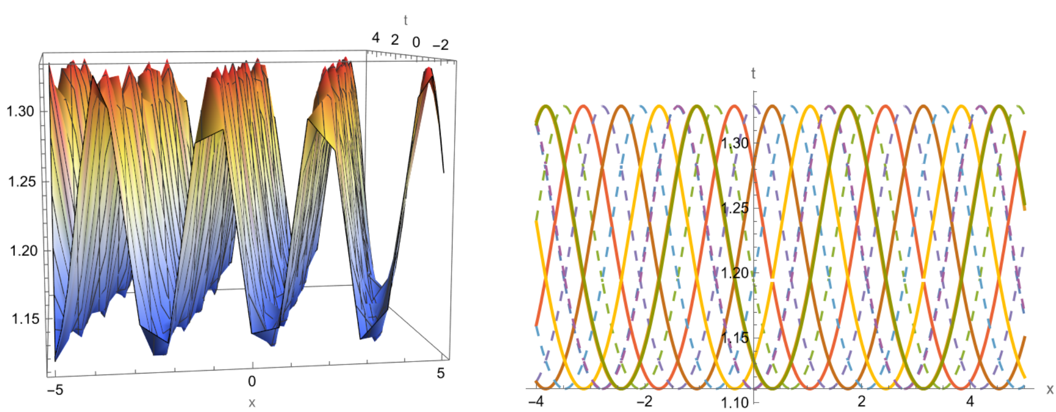


Figure 7: The visual plot of $\varpi(x,t)$ described in equation (31) can be obtained by setting $\Xi = 1.6$, $\Gamma = 0.81$, $\varsigma_1 = 1.51$, $\varsigma_2 = 1.5$, $\psi = 0.5$, $\mu_0 = 0$, $p = 0$, and $\kappa = 1.2$.

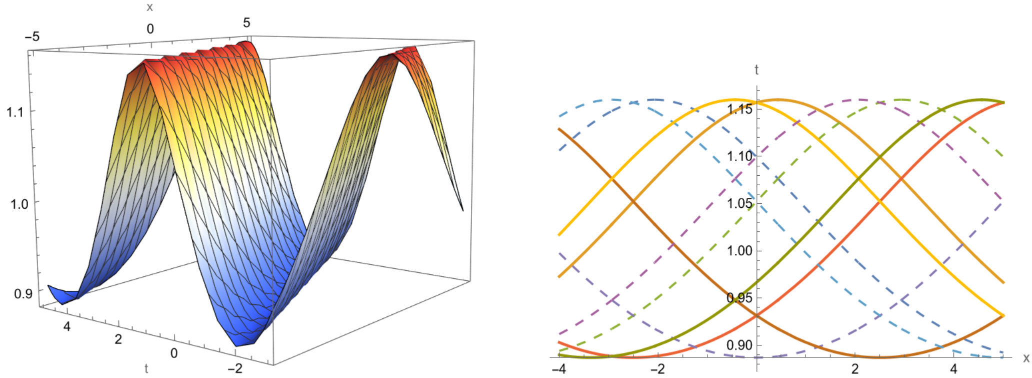


Figure 8: When $\Xi = 1.5$, $\Gamma = 0.51$, $\varsigma_1 = 1.31$, $\varsigma_2 = 1.3$, $\psi = 0.5$, $\mu_0 = 0$, $p = 0$, $\kappa = 0.8$, the visual plot of $\varpi(x,t)$ as depicts in equation (32).

**Case 4:** $D_2 > 0$, $D_3 = 0$, $D_4 = 0$, and $E_2 = 0$. Thus, we have

$$F(\Lambda) = (\Lambda - \Upsilon)^3(\Lambda - \varepsilon). \tag{33}$$

Hence, we have

$$\Lambda = \frac{4(\Upsilon - \varepsilon)}{(\varepsilon - \Upsilon)^2(\frac{-F}{2})(\mu - \mu_0)^2 - 4} + \Upsilon, \tag{34}$$

$$\Lambda = \frac{4(\Upsilon - \varepsilon)}{-(\varepsilon - \Upsilon)^2(\frac{-F}{2})(\mu - \mu_0)^2 - 4} + \Upsilon. \tag{35}$$

Since, we get the two solutions

$$\varpi(x,t) = \left(\frac{4(\Upsilon - \varepsilon)}{(\varepsilon - \Upsilon)^2(\frac{-F}{2})(\mu - \mu_0)^2 - 4} + \Upsilon\right) \exp^{\left[i\left(-\kappa t + \psi x + p\right)\right]}, \tag{36}$$

$$\varpi(x,t) = \left(\frac{4(\Upsilon - \varepsilon)}{-(\varepsilon - \Upsilon)^2(\frac{-F}{2})(\mu - \mu_0)^2 - 4} + \Upsilon\right) \exp^{\left[i\left(-\kappa t + \psi x + p\right)\right]}, \tag{37}$$

that are a rational solutions.

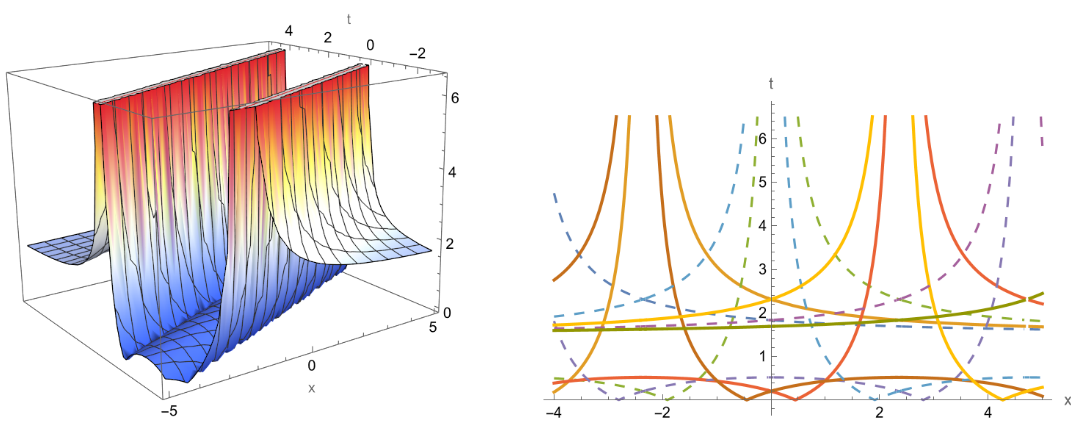


Figure 9: When $\Upsilon = 1.5$, $\varepsilon = 0.52$, $\varsigma_1 = 1.33$, $\varsigma_2 = 1.31$, $\psi = 0.5$, $\mu_0 = 0$, $p = 0$, $\kappa = 0.81$, the dynamics of $\varpi(x,t)$ as depicts in equation (36).

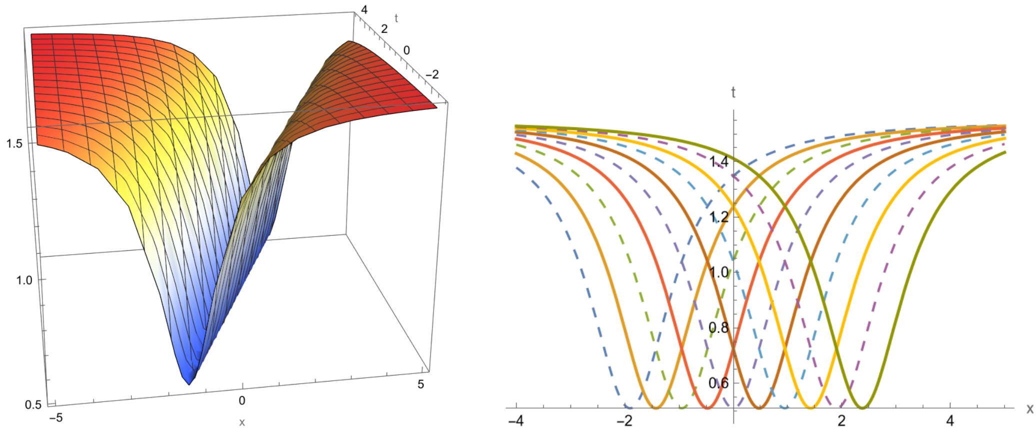


Figure 10: When $\Upsilon = 1.55$, $\varepsilon = 0.51$, $\varsigma_1 = 0.33$, $\varsigma_2 = 1.34$, $\psi = 0.52$, $\mu_0 = 0$, $p = 0$, $\kappa = 0.81$, the visual representation of $\varpi(x,t)$ as depicts in equation (37).

**Case 5:** $D_2D_3 < 0$, and $D_4 = 0$. Since,

$$F(\Lambda) = (\Lambda - \Xi)^2\Big((\Lambda - M)^2 + N^2\Big). \tag{38}$$

Then, we have

$$\Lambda = \frac{\left(\exp^{\pm\sqrt{(\Xi-M)^2+N^2}\sqrt{\frac{-F}{2}}(\mu-\mu_0)} - \delta\right) + \sqrt{(\Xi - M)^2 + N^2}(2-\delta)}{\left(\exp^{\pm\sqrt{(\Xi-M)^2+N^2}\sqrt{\frac{-F}{2}}(\mu-\mu_0)} - \delta\right)^2 - 1}, \tag{39}$$

where $\delta = \dfrac{\Xi - 2M}{\sqrt{(\Xi - M)^2 + N^2}}$. Consequently, we get the solution

$$\varpi(x,t) = \frac{\left(\exp^{\pm\sqrt{(\Xi-M)^2+N^2}\sqrt{\frac{-F}{2}}(\mu-\mu_0)} - \delta\right) + \sqrt{(\Xi - M)^2 + N^2}(2-\delta)}{\left(\exp^{\pm\sqrt{(\Xi-M)^2+N^2}\sqrt{\frac{-F}{2}}(\mu-\mu_0)} - \delta\right)^2 - 1}\exp^{\left[i\left(-\kappa t+\psi x+p\right)\right]}, \tag{40}$$

which is a solitary wave solution.

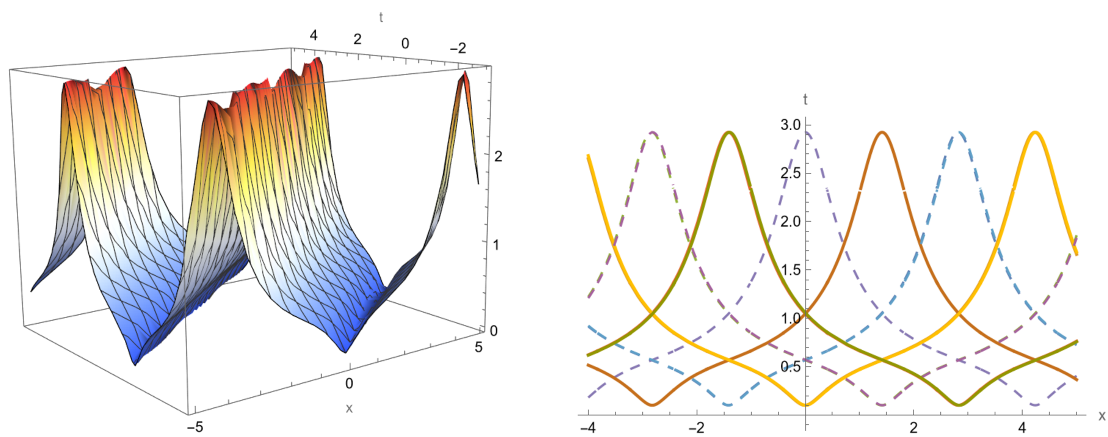


Figure 11: When $\Xi = 1.56$, $M = 0.53$, $N = 0.2$, $\varsigma_1 = 0.34$, $\varsigma_2 = 1.35$, $\psi = 0.54$, $\mu_0 = 0$, $p = 0$, $\kappa = 0.51$, the figure of $\varpi(x,t)$ as express in equation (40).

**Case 6:** $D_2 > 0$, $D_3 > 0$, and $D_4 > 0$. Since, we have

$$F(\Lambda) = (\Lambda - \eta_1)(\Lambda - \eta_2)(\Lambda - \eta_3)(\Lambda - \eta_4). \tag{41}$$

Therefore, we have

$$\Lambda = \frac{\eta_3(\eta_1-\eta_2)sn^2\left(\frac{\sqrt{(\eta_1-\eta_3)(\eta_2-\eta_4)}}{2}\sqrt{\frac{-F}{2}}(\mu-\mu_0),\alpha\right)-\eta_2(\eta_1-\eta_3)}{(\eta_1-\eta_2)sn^2\left(\frac{\sqrt{(\eta_1-\eta_3)(\eta_2-\eta_4)}}{2}\sqrt{\frac{-F}{2}}(\mu-\mu_0),\alpha\right)-(\eta_1-\eta_3)}, \tag{42}$$

$$\Lambda = \frac{\eta_1(\eta_3-\eta_4)sn^2\left(\frac{\sqrt{(\eta_1-\eta_3)(\eta_2-\eta_4)}}{2}\sqrt{\frac{-F}{2}}(\mu-\mu_0),\alpha\right)-\eta_4(\eta_3-\eta_1)}{(\eta_3-\eta_4)sn^2\left(\frac{\sqrt{(\eta_1-\eta_3)(\eta_2-\eta_4)}}{2}\sqrt{\frac{-F}{2}}(\mu-\mu_0),\alpha\right)-(\eta_3-\eta_1)}, \tag{43}$$

where $\alpha = \dfrac{(\eta_1-\eta_2)(\eta_3-\eta_4)}{(\eta_1-\eta_3)(\eta_2-\eta_4)}$. Since, we get the two solutions

$$\varpi(x,t) = \frac{\eta_3(\eta_1-\eta_2)sn^2\left(\frac{\sqrt{(\eta_1-\eta_3)(\eta_2-\eta_4)}}{2}\sqrt{\frac{-F}{2}}(\mu-\mu_0),\alpha\right)-\eta_2(\eta_1-\eta_3)}{(\eta_1-\eta_2)sn^2\left(\frac{\sqrt{(\eta_1-\eta_3)(\eta_2-\eta_4)}}{2}\sqrt{\frac{-F}{2}}(\mu-\mu_0),\alpha\right)-(\eta_1-\eta_3)}\exp^{\left[i\left(-\kappa t+\psi x+p\right)\right]}, \tag{44}$$

$$\varpi(x,t) = \frac{\eta_1(\eta_3-\eta_4)sn^2\left(\frac{\sqrt{(\eta_1-\eta_3)(\eta_2-\eta_4)}}{2}\sqrt{\frac{-F}{2}}(\mu-\mu_0),\alpha\right)-\eta_4(\eta_3-\eta_1)}{(\eta_3-\eta_4)sn^2\left(\frac{\sqrt{(\eta_1-\eta_3)(\eta_2-\eta_4)}}{2}\sqrt{\frac{-F}{2}}(\mu-\mu_0),\alpha\right)-(\eta_3-\eta_1)}\exp^{\left[i\left(-\kappa t+\psi x+p\right)\right]}, \tag{45}$$

that are a elliptic function double periodic solutions.

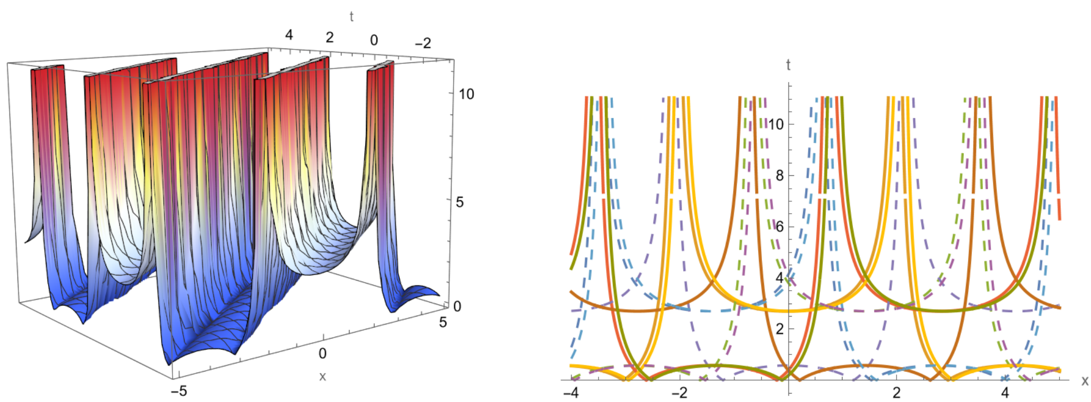

Figure 12: When $\eta_1 = 1.59$, $\eta_2 = 0.58$, $\eta_3 = 1.6$, $\eta_4 = 2.7$, $\varsigma_1 = 0.37$, $\varsigma_2 = 1.39$, $\psi = 0.49$, $\mu_0 = 0$, $p = 0$, $\kappa = 0.51$, the shape of $\varpi(x,t)$ as display in equation (44).

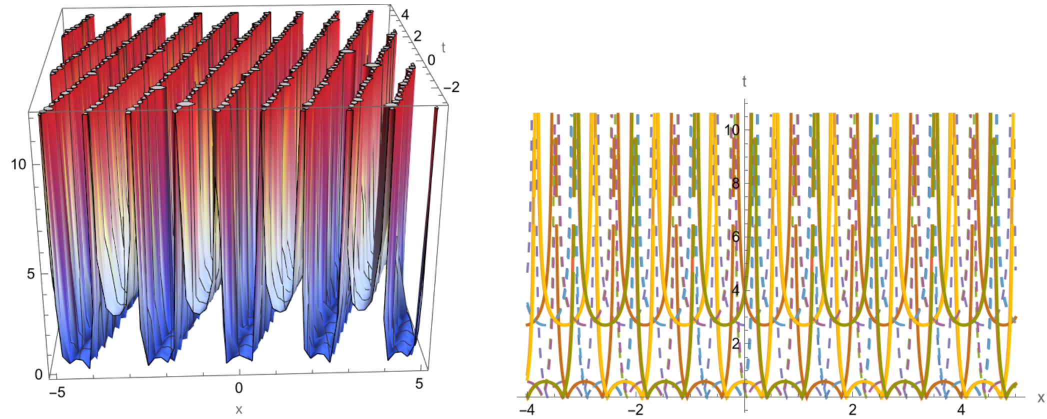


Figure 13: When $\eta_1 = 1.58$, $\eta_2 = 0.59$, $\eta_3 = 1.6$, $\eta_4 = 2.7$, $\varsigma_1 = 0.36$, $\varsigma_2 = 1.39$, $\psi = 0.49$, $\mu_0 = 0$, $p = 0$, $\kappa = 0.9$, the visual dynamics of $\varpi(x,t)$ as present in equation (44).

**Case 7:** $D_2D_3 \geq 0$, and $D_4 < 0$. So, we have

$$F(\Lambda) = (\Lambda - \vartheta)(\Lambda - \xi)\Big((\Lambda - \sigma)^2 + K^2\Big), \tag{46}$$

where $\vartheta > \xi$, $K > 0$, $\sigma > 0$. We denote

$$\begin{aligned} P &= \frac{1}{2}(\vartheta + \xi)n - \frac{1}{2}(\vartheta - \xi)f, \\ Q &= \frac{1}{2}(\vartheta + \xi)f - \frac{1}{2}(\vartheta - \xi)n, \\ R &= \vartheta - \sigma - \frac{K}{\upsilon_1}, \\ S &= \vartheta - \sigma - K\upsilon_1, \\ G &= \frac{K^2 + (\vartheta - \sigma)(\vartheta - \xi)}{K(\vartheta - \xi)}, \\ \alpha_1 &= G \pm \sqrt{G^2 + 1}, \\ \alpha^2 &= \frac{1}{1 + \alpha_1}. \end{aligned} \tag{47}$$

Then, we have

$$\Lambda = \frac{Pcn\Big(\frac{\sqrt{\mp 2K\alpha_1(\vartheta - \xi)}}{2\alpha\alpha_1}\sqrt{\frac{-F}{2}}(\mu - \mu_0), \alpha\Big) + Q}{Rcn\Big(\frac{\sqrt{\mp 2K\alpha_1(\vartheta - \xi)}}{2\alpha\alpha_1}\sqrt{\frac{-F}{2}}(\mu - \mu_0), \alpha\Big) + S}. \tag{48}$$

Therefore, we get the solution

$$\varpi(x,t) = \frac{Pcn\Big(\frac{\sqrt{\mp 2K\alpha_1(\vartheta - \xi)}}{2\alpha\alpha_1}\sqrt{\frac{-F}{2}}(\mu - \mu_0), \alpha\Big) + Q}{Rcn\Big(\frac{\sqrt{\mp 2K\alpha_1(\vartheta - \xi)}}{2\alpha\alpha_1}\sqrt{\frac{-F}{2}}(\mu - \mu_0), \alpha\Big) + S}\exp^{\left[i\left(-\kappa t + \psi x + p\right)\right]}, \tag{49}$$

which is a elliptic function double periodic solution.

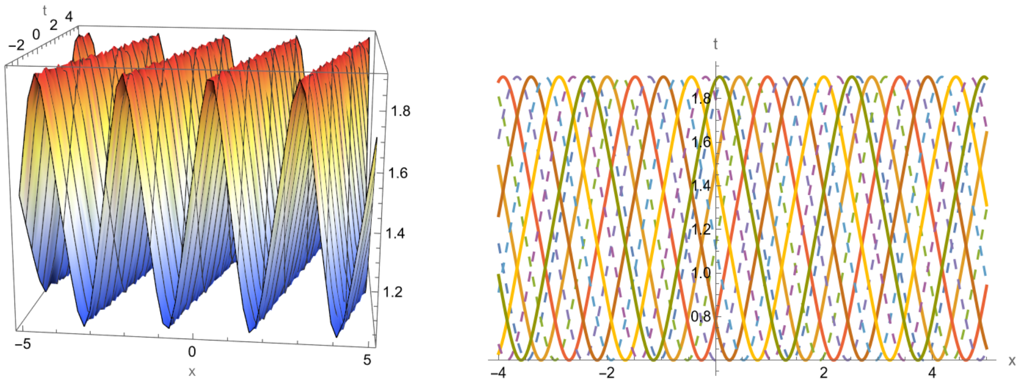


Figure 14: When $\vartheta = 1.9$, $\xi = 0.6$, $\sigma = 1.6$, $K = 0.7$, $\varsigma_1 = 1.5$, $\varsigma_2 = 2.7$, $\psi = 0.7$, $\mu_0 = 0$, $p = 0$, $\kappa = 0.9$, the visual display of $\varpi(x, t)$ as shown in equation (49).

**Case 8:** $D_2 D_3 \leq 0$, and $D_4 > 0$. So, we have

$$F(\Lambda) = \Big((\Lambda - d_1)^2 + e_1^2\Big)\Big((\Lambda - d_2)^2 + e_2^2\Big), \tag{50}$$

where $e_1 \geq e_2 > 0$. We denote

$$\begin{aligned}
R &= d_1 T + e_1 U, \\
S &= d_1 U - e_1 T, \\
T &= -e_1 - \frac{e_2}{\upsilon_1}, \\
U &= d_1 - d_2, \\
H &= \frac{(d_1 - d_2)^2 + e_1^2 + e_2^2}{2 e_1 e_2}, \\
\alpha_1 &= H + \sqrt{H^2 - 1}, \\
\alpha^2 &= \frac{\alpha_1^2 - 1}{\alpha_1^2}.
\end{aligned} \tag{51}$$

Then, we have

$$\Lambda = \frac{Rsn\Big(\nu\sqrt{\frac{-F}{2}}(\mu - \mu_0), \alpha\Big) + Scn\Big(\nu\sqrt{\frac{-F}{2}}(\mu - \mu_0), \alpha\Big)}{Tsn\Big(\nu\sqrt{\frac{-F}{2}}(\mu - \mu_0), \alpha\Big) + Ucn\Big(\nu\sqrt{\frac{-F}{2}}(\mu - \mu_0), \alpha\Big)}, \tag{52}$$

where $\nu = \dfrac{e_2\sqrt{(T^2 + U^2)(\alpha_1^2 T^2 + U^2)}}{T^2 + U^2}$. Therefore, we get the solution

$$\varpi(x, t) = \frac{Rsn\Big(\nu\sqrt{\frac{-F}{2}}(\mu - \mu_0), \alpha\Big) + Scn\Big(\nu\sqrt{\frac{-F}{2}}(\mu - \mu_0), \alpha\Big)}{Tsn\Big(\nu\sqrt{\frac{-F}{2}}(\mu - \mu_0), \alpha\Big) + Ucn\Big(\nu\sqrt{\frac{-F}{2}}(\mu - \mu_0), \alpha\Big)} \exp^{\left[i\left(-\kappa t + \psi x + p\right)\right]}, \tag{53}$$

which is a elliptic function double periodic solution.

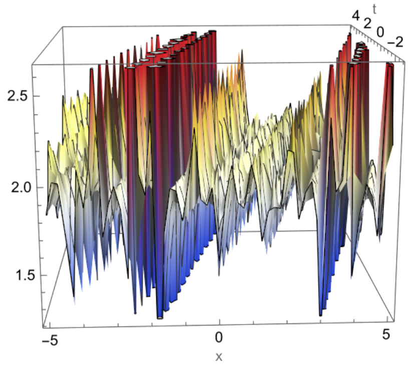


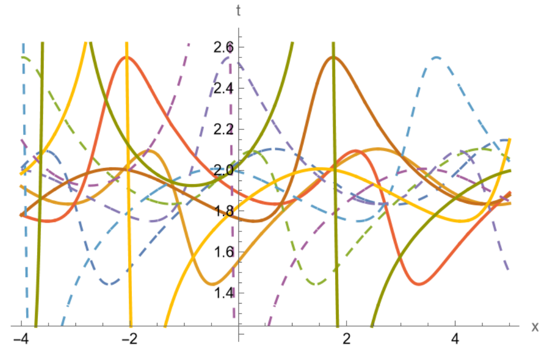


Figure 15: When $d_1 = 1.9, d_2 = 2.7, e_1 = 0.6, e_2 = 1.6, \varsigma_1 = 1.5, \varsigma_2 = 2.7, \psi = 0.7, \mu_0 = 0, p = 0, \kappa = 0.5$, the visual representation of $\varpi(x, t)$ as depicted in equation (53) is displayed.

The aforementioned findings show that applying the CDSPM allows us to easily design different kinds of explicit solutions while obtaining the essential area.

## 4 Application of CDS for Third Degree Polynomial

Now after applying substituting $\Lambda^2 = \rho$ to equation (9), then we get the equation:

$$(\rho')^2 + \frac{F}{2}\rho^3 - E\rho^2 + 2C\rho = 0, \tag{54}$$

$$(\rho')^2 = -\frac{F}{2}(\rho^3 + v_2\rho^2 + v_1\rho + v_0), \tag{55}$$

where,

$$v_2 = \frac{2E}{F}, \qquad v_1 = \frac{4C}{F}, \qquad v_0 = 0. \tag{56}$$

We only consider the case when $F < 0$ in equation (55); however, the case where $F > 0$ may be considered in a similar manner [17]. In equation (55)'s integral form, we have

$$\int \frac{d\rho}{\sqrt{\rho^3 + v_2\rho^2 + v_1\rho + v_0}} = \pm\sqrt{\frac{F}{2}}(\mu - \mu_0), \tag{57}$$

where $\mu_0$ is constant of integration. Now, denote $F(\rho) = \rho^3 + v_2\rho^2 + v_1\rho + v_0$ and CDS as follows,

$$\Delta = -27\left(\frac{2}{27}v_2^3 + v_0 - \frac{v_1v_2}{3}\right)^2 - 4\left(v_1 - \frac{v_2^2}{3}\right)^3, \qquad D = v_1 - \frac{1}{3}v_2^2. \tag{58}$$

As may be seen, the dynamic system below is equal to equation (57),

$$\begin{cases} \rho' = \beta(\mu), \\ \beta' = -\dfrac{F}{4}\left(3\rho^2 + 2v_2\rho + v_1\right), \end{cases} \tag{59}$$

the Hamiltonian of the system is stated as follows,

$$H(\rho, \beta) = \frac{\beta^2}{2} + \frac{F}{4}\Big(\rho^3 + v_2\rho^2 + v_1\rho + v_0\Big). \tag{60}$$

The potential energy may thus be written as,

$$U(\rho) = \frac{F}{4}\Big(\rho^3 + v_2\rho^2 + v_1\rho + v_0\Big). \tag{61}$$

### 4.1 Qualitative analysis.

Computing the roots of $U'(\rho)$ is required in order to analyse the dynamic features of equation (57), [17],

$$U'(\rho) = \frac{3F}{4}\Big(\rho^2 + I_1\rho + I_0\Big), \tag{62}$$

where $I_1 = \frac{2v_2}{3}$ and $I_0 = \frac{v_1}{3}$, whose CDS is given by

$$\Delta = \frac{9F^2 I_1^2}{16} - \frac{9F^2 I_0}{4}. \tag{63}$$

The CDSPM must be used to discuss three situations in accordance with the form of $U'(\rho)$.

**Case 1:** $\Delta < 0$,

$$U'(\rho) = \frac{3F}{4}\Big(\rho^2 + 2c_1\rho + c_1^2 c_2^2\Big). \tag{64}$$

There is no equilibrium point for the dynamic system in this situation. The global phase depicts at $c_1 = 1$, $c_2 = 1.4$ and $F = \pm 1$ are shown in Figure 16.

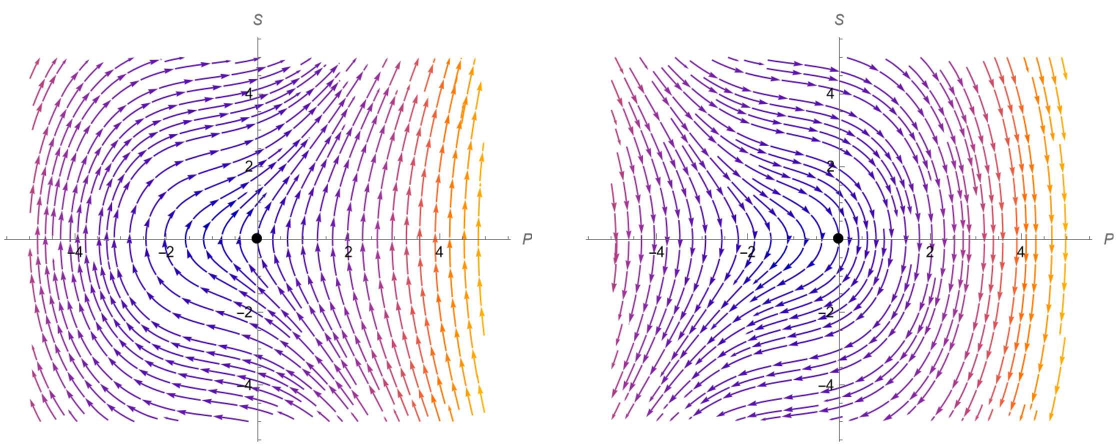


Figure 16: In Case 1, the behavior of the System 59 is illustrated by its phase portraits: (a) $F = 1$, (b) $F = -1$.

**Case 2:** $\Delta = 0$,

$$U'(\rho) = \frac{3F}{4}\Big(\rho - \iota_1\Big)^2. \tag{65}$$

In this situation, a cuspidal point in the dynamic system may be found at $(\iota_1, 0)$. The global phase illustrations for $\iota_1 = 1$ and $F = \pm 1$ are shown in Figure 17.

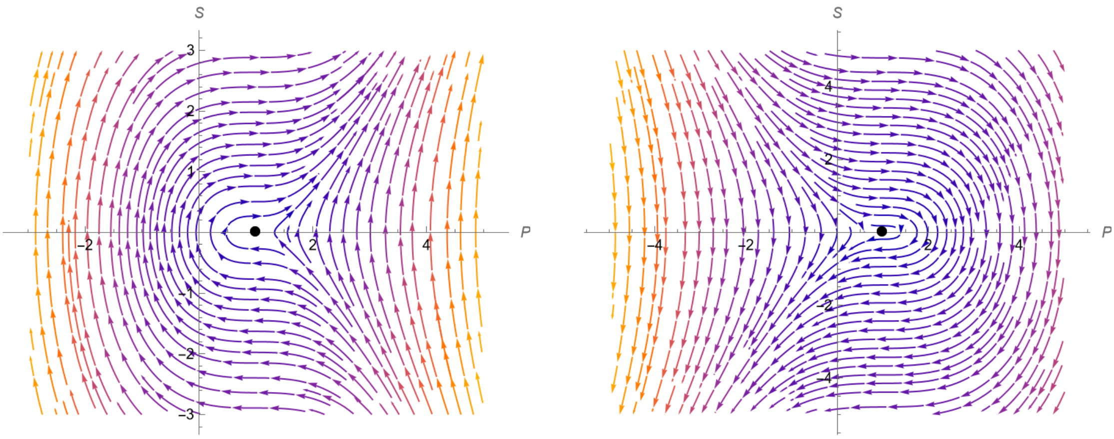


Figure 17: The behavior of the System 59 in Case 2 is represented by its phase portraits: (a) $F = 1$, (b) $F = -1$.

**Case 3:** $\Delta > 0$,

$$U'(\rho) = \frac{3F}{4}\Big(\rho - b_1\Big)\Big(\rho - b_2\Big). \tag{66}$$

There are two points of equilibrium. The given case for the dynamic system has $(b_1, 0)$ and $(b_2, 0)$, with $(b_1, 0)$ being a centre and $(b_2, 0)$ being a saddle point. The global phase portraits are shown in Figure 18 for $b_1 = -3.4$, $b_2 = -0.5$ and $F = \pm 1$.

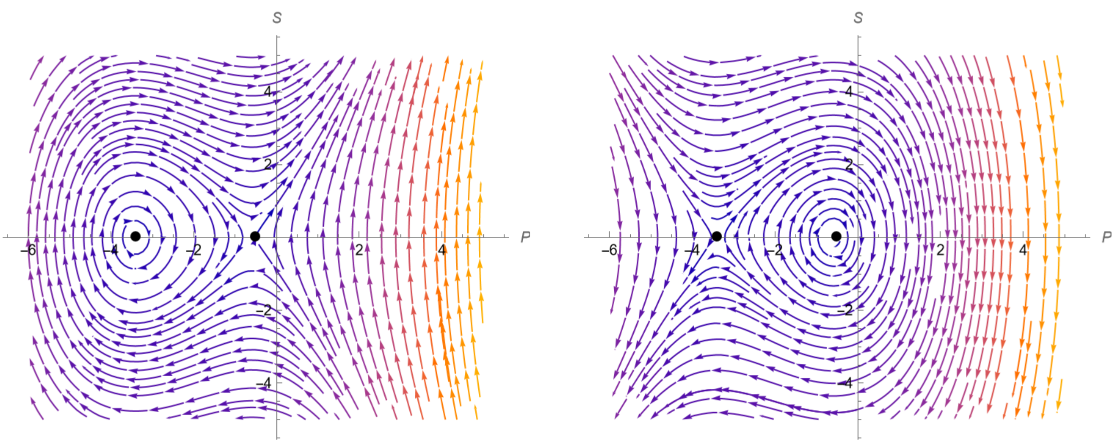


Figure 18: In Case 3, the behavior of the System 59 is illustrated by its phase portraits: (a) $F = 1$, (b) $F = -1$.

The results show that the modification of parameters, particularly the equilibrium points, has a considerable impact on the dynamic characteristics. The CDSPM may be used to quickly analyze a wide range of equilibrium points and bifurcations.

### 4.2 Exact solutions

The previous findings confirmed the existence of periodic and soliton solutions. Moving on, we want to determine the exact answer using CDSPM[17]. The full list of all solutions is provided below.

**Case 1:** $\Delta = 0$, $D < 0$, that are in equation (58). Then we have

$$F(\rho) = (\rho - \chi)^2(\rho - \gamma), \qquad \chi \neq \gamma. \tag{67}$$

If $\rho > \gamma$, the solutions are given as follows,

$$\Lambda = \sqrt{(\chi - \gamma)\tanh^2\left(\frac{\sqrt{\chi - \gamma}}{2}\sqrt{\frac{-F}{2}}(\mu - \mu_0)\right) + \gamma}, \qquad \chi > \gamma, \tag{68}$$

$$\Lambda = \sqrt{(\chi - \gamma)\coth^2\left(\frac{\sqrt{\chi - \gamma}}{2}\sqrt{\frac{-F}{2}}(\mu - \mu_0)\right) + \gamma}, \qquad \chi > \gamma, \tag{69}$$

$$\Lambda = \sqrt{(\chi - \gamma)\tan^2\left(\frac{\sqrt{\chi - \gamma}}{2}\sqrt{\frac{-F}{2}}(\mu - \mu_0)\right) + \gamma}, \qquad \chi < \gamma. \tag{70}$$

Based on the preceding outcomes, we obtain the following three solutions,

$$\varpi(x,t) = \sqrt{(\chi - \gamma)\tanh^2\left(\frac{\sqrt{\chi - \gamma}}{2}\sqrt{\frac{-F}{2}}(\mu - \mu_0)\right) + \gamma}\, \exp^{\left[i\left(-\kappa t + \psi x + p\right)\right]}, \tag{71}$$

$$\varpi(x,t) = \sqrt{(\chi - \gamma)\coth^2\left(\frac{\sqrt{\chi - \gamma}}{2}\sqrt{\frac{-F}{2}}(\mu - \mu_0)\right) + \gamma}\, \exp^{\left[i\left(-\kappa t + \psi x + p\right)\right]}, \tag{72}$$

$$\varpi(x,t) = \sqrt{(\chi - \gamma)\tan^2\left(\frac{\sqrt{\chi - \gamma}}{2}\sqrt{\frac{-F}{2}}(\mu - \mu_0)\right) + \gamma}\, \exp^{\left[i\left(-\kappa t + \psi x + p\right)\right]}. \tag{73}$$

Equations (71) and (72) is a solitary wave solution and equation (73) is a periodic solution.

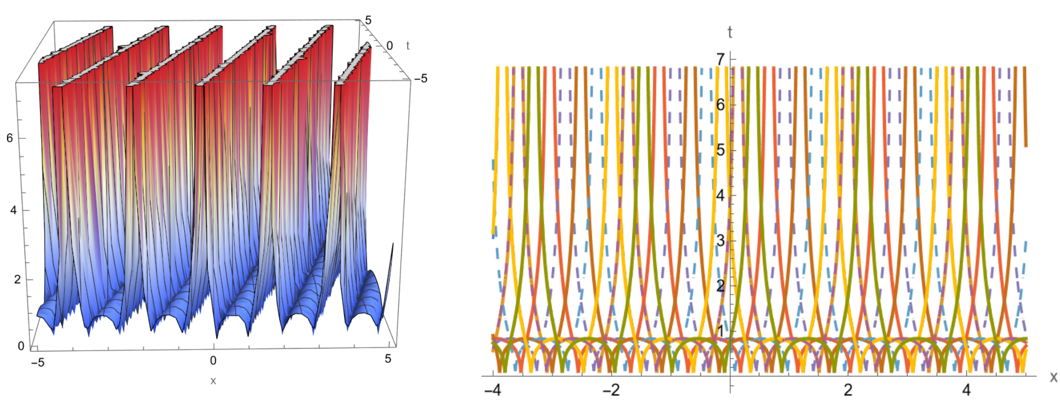


Figure 19: Plot the $\varpi(x,t)$ in equation (71) at $\chi = 1.5$, $\gamma = 0.7$, $\varsigma_1 = 1$, $\varsigma_2 = 2.3$, $\psi = 0.7$, $\mu_0 = 0$, $p = 0$, $\kappa = 0.9$.

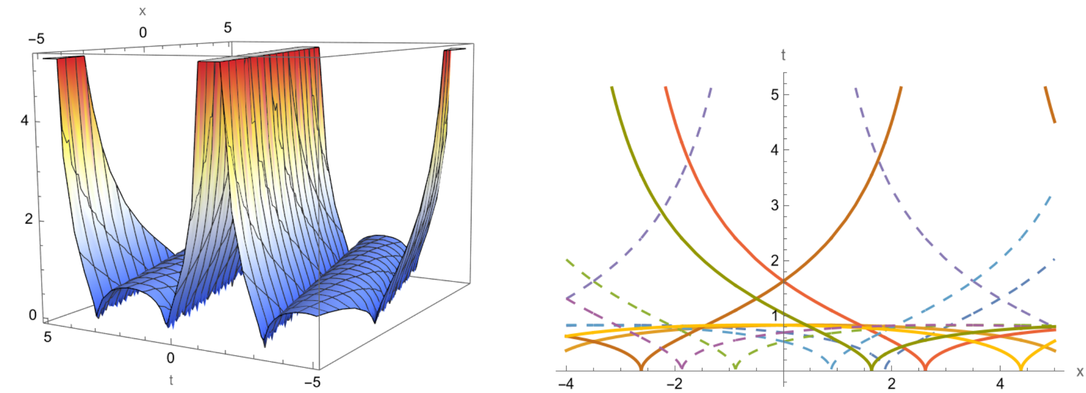


Figure 20: The dynamics $\varpi(x,t)$ in equation (72) when $\chi = 1.7$, $\gamma = 0.7$, $\varsigma_1 = 1.1$, $\varsigma_2 = 2.1$, $\psi = 0.6$, $\mu_0 = 0$, $p = 0$, $\kappa = 0.45$.

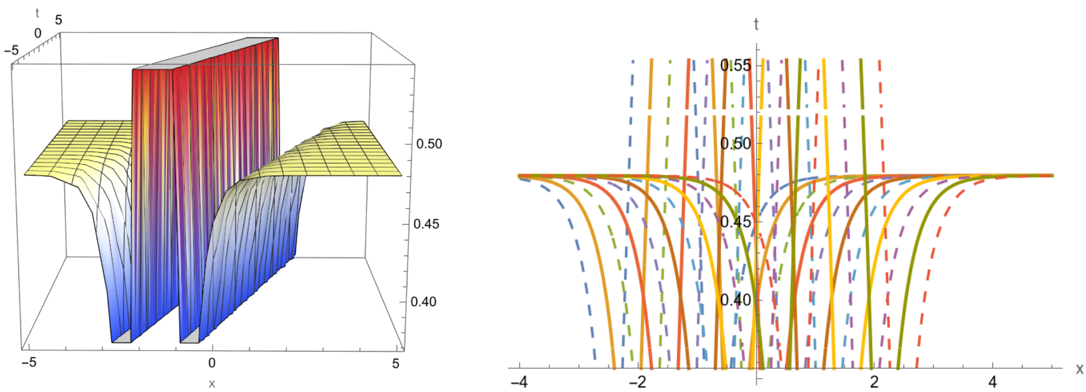


Figure 21: The representation of $\varpi(x,t)$ in equation (73) is graphically displayed as when $\chi = 1.69$, $\gamma = 0.73$, $\varsigma_1 = 1.2$, $\varsigma_2 = 2.2$, $\psi = 0.6$, $\mu_0 = 0$, $p = 0$, $\kappa = 0.9$.

**Case 2:** $\Delta > 0$, $D < 0$, that are in equation (58). Then we have

$$F(\rho) = (\rho - \Theta)^3. \tag{74}$$

Hence, we have

$$\Lambda = \sqrt{\frac{-8}{F}(\mu - \mu_0)^{-2} + \Theta}. \tag{75}$$

Furthermore, we obtain the solution

$$\varpi(x,t) = \sqrt{\frac{-8}{F}(\mu - \mu_0)^{-2} + \Theta}\exp^{\left[i\left(-\kappa t + \psi x + p\right)\right]}. \tag{76}$$

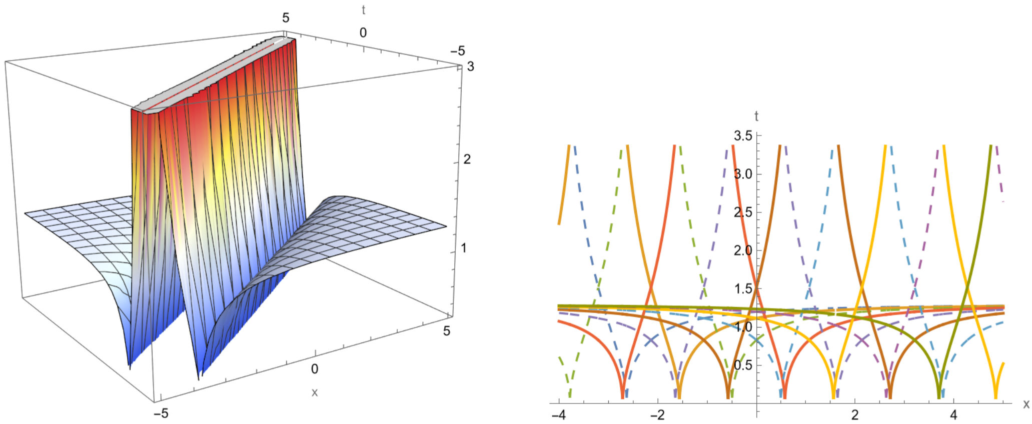

Figure 22: When $\Theta = 1.69$, $\varsigma_1 = 1.2$, $\varsigma_2 = 2.2$, $\psi = 0.6$, $\mu_0 = 0$, $p = 0.003$, $\kappa = 0.6$, then the equation (76) for $\varpi(x,t)$ can be visually expressed through a figure.

**Case 3:** $\Delta > 0$, $D < 0$, that are in equation (58). Then we have,

$$F(\rho) = (\rho - \zeta)(\rho - \eta)(\rho - \theta), \tag{77}$$

we consider $\zeta < \eta < \theta$. When $\zeta < \rho < \eta$, we have

$$\Lambda = \sqrt{\zeta + (\eta - \zeta) sn^2\left(\frac{\sqrt{\theta - \zeta}}{2}\sqrt{\frac{-F}{2}}(\mu - \mu_0), \alpha\right)}. \tag{78}$$

When $\rho > \theta$,

$$\Lambda = \sqrt{\frac{\theta - \eta sn^2\left(\frac{\sqrt{\theta-\zeta}}{2}\sqrt{\frac{-F}{2}}(\mu - \mu_0), \alpha\right)}{cn^2\left(\frac{\sqrt{\theta-\zeta}}{2}\sqrt{\frac{-F}{2}}(\mu - \mu_0), \alpha\right)}}, \tag{79}$$

where $\alpha = \dfrac{\eta - \zeta}{\theta - \zeta}$. Consequently, we obtain two solutions

$$\varpi(x,t) = \sqrt{\zeta + (\eta - \zeta) sn^2\left(\frac{\sqrt{\theta - \zeta}}{2}\sqrt{\frac{-F}{2}}(\mu - \mu_0), \alpha\right)} \exp^{\left[i\left(-\kappa t + \psi x + p\right)\right]}, \tag{80}$$

$$\varpi(x,t) = \sqrt{\frac{\theta - \eta sn^2\left(\frac{\sqrt{\theta-\zeta}}{2}\sqrt{\frac{-F}{2}}(\mu - \mu_0), \alpha\right)}{cn^2\left(\frac{\sqrt{\theta-\zeta}}{2}\sqrt{\frac{-F}{2}}(\mu - \mu_0), \alpha\right)}} \exp^{\left[i\left(-\kappa t + \psi x + p\right)\right]}. \tag{81}$$

Equations (80) and (81) are the elliptic function solution.

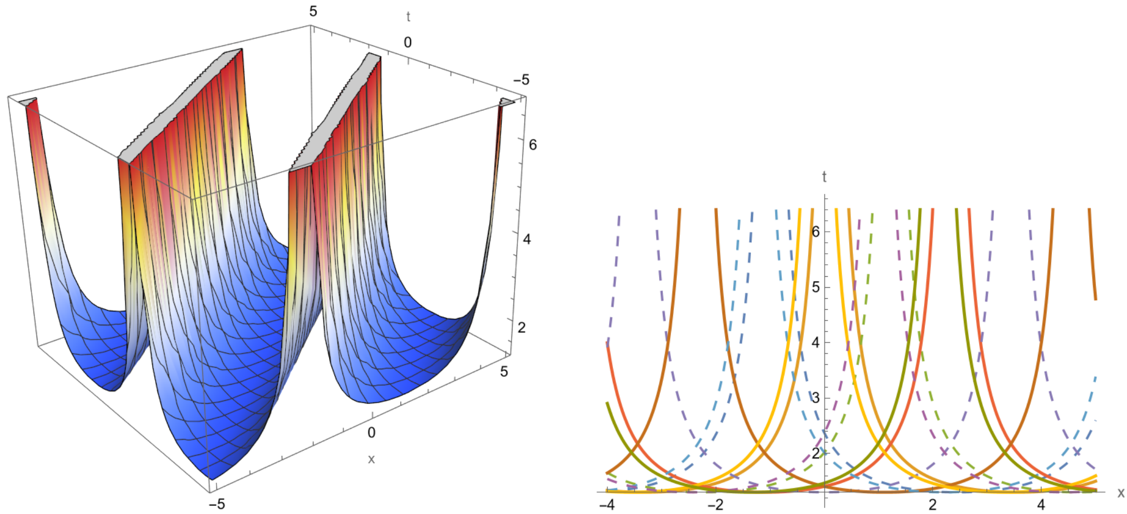


Figure 23: When $\zeta = 1.69$, $\eta = 0.713$, $\theta = 0.8$, $\varsigma_1 = 1.1$, $\varsigma_2 = 2.12$, $\psi = 0.61$, $\mu_0 = 0$, $p = 0$, $\kappa = 0.61$, then the equation (80) produces a visual plot of $\varpi(x,t)$.

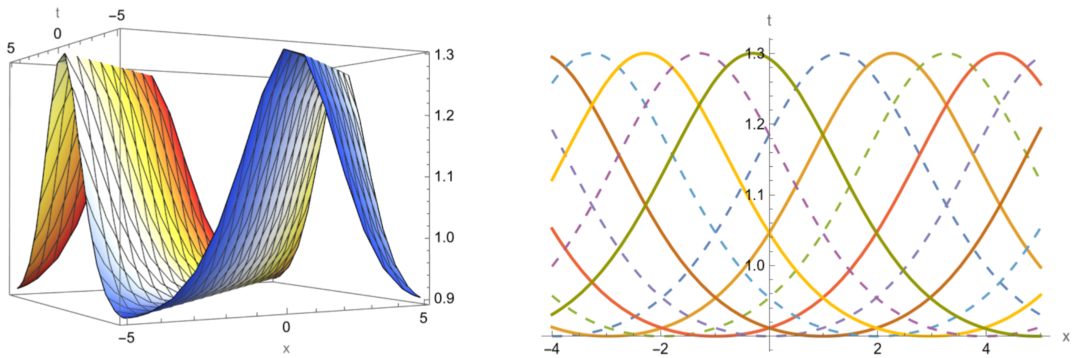


Figure 24: When $\zeta = 1.691$, $\eta = 0.72$, $\theta = 0.81$, $\varsigma_1 = 1.2$, $\varsigma_2 = 2.12$, $\psi = 0.62$, $\mu_0 = 0$, $p = 0$, $\kappa = 0.63$, then the equation (81) shows a visual depiction of $\varpi(x,t)$.

**Case 4:** $\Delta < 0$, that is in equation (58). Then we have

$$F(\rho) = (\rho - \pi)(\rho^2 + gm + h), \qquad g^2 - 4h < 0. \tag{82}$$

Since, we have

$$\Lambda = \sqrt{\pi - \sqrt{\pi^2 + g\pi + h} + \frac{2\sqrt{\pi^2 + g\pi + h}}{1 + cn\left((\pi^2 + g\pi + h)^{\frac{1}{4}}\sqrt{\frac{-F}{2}}(\mu - \mu_0), \alpha\right)}}, \tag{83}$$

where $\alpha = \frac{1}{2}\left(1 - \frac{\pi + \frac{g}{2}}{\sqrt{\pi^2 + g\pi + h}}\right)$. Furthermore, we obtain the solution

$$\varpi(x,t) = \sqrt{\pi - \sqrt{\pi^2 + g\pi + h} + \frac{2\sqrt{\pi^2 + g\pi + h}}{1 + cn\left((\pi^2 + g\pi + h)^{\frac{1}{4}}\sqrt{\frac{-F}{2}}(\mu - \mu_0), \alpha\right)}}\, \exp^{\left[i\left(-\kappa t + \psi x + p\right)\right]}. \tag{84}$$

Equation (84) is also the elliptic function solution.

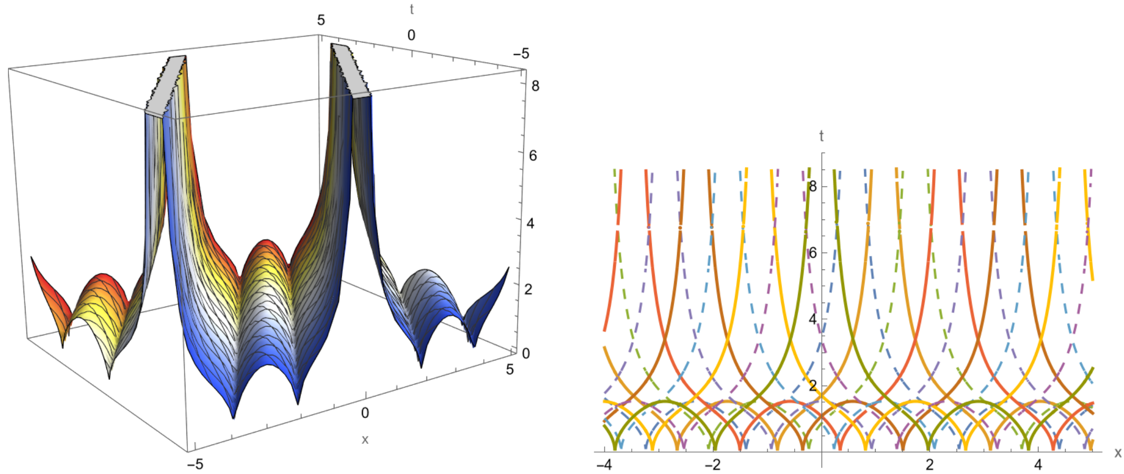


Figure 25: When $\phi = 1.68$, $g = 0.3$, $h = 0.7$, $\varsigma_1 = 1.5$, $\varsigma_2 = 2.15$, $\psi = 0.64$, $\mu_0 = 0$, $p = 0$, $\kappa = 0.8$, then the equation (84) depicts a graph of $\varpi(x,t)$.

The results show that adopting the CDSPM allows us to obtain the essential region and easily create various sorts of solutions in explicit form.

## 5 The SW Solutions

It's fascinating to investigate alternate explicit and exact local pulse solutions that propagate in a fibre optic system. Here, we find SW solution by converting JEF into hyperbolic and trigonometric functions. The JEF converted into hyperbolic functions and trigonometric functions at the long-wave limit, which approach to $\alpha \to 0$ and $\alpha \to 1$ respectively.

### 5.1 Double hyperbolic-I SW

By taking the limit $\alpha \to 1$ in equation (44) and equation (45), then the function degenerate into

$$sn^2\left(\frac{\sqrt{(\eta_1-\eta_3)(\eta_2-\eta_4)}}{2}\sqrt{\frac{-F}{2}}(\mu-\mu_0),\alpha\right) \to \tanh^2\left(\frac{\sqrt{(\eta_1-\eta_3)(\eta_2-\eta_4)}}{2}\sqrt{\frac{-F}{2}}(\mu-\mu_0)\right),$$

which present the SWs solution[15]:

$$\varpi(x,t) = \frac{\eta_3(\eta_1-\eta_2)\tanh^2\left(\frac{\sqrt{(\eta_1-\eta_3)(\eta_2-\eta_4)}}{2}\sqrt{\frac{-F}{2}}(\mu-\mu_0)\right)-\eta_2(\eta_1-\eta_3)}{(\eta_1-\eta_2)\tanh^2\left(\frac{\sqrt{(\eta_1-\eta_3)(\eta_2-\eta_4)}}{2}\sqrt{\frac{-F}{2}}(\mu-\mu_0)\right)-(\eta_1-\eta_3)}\exp^{\left[i\left(-\kappa t+\psi x+p\right)\right]}, \tag{85}$$

$$\varpi(x,t) = \frac{\eta_1(\eta_3-\eta_4)\tanh^2\left(\frac{\sqrt{(\eta_1-\eta_3)(\eta_2-\eta_4)}}{2}\sqrt{\frac{-F}{2}}(\mu-\mu_0)\right)-\eta_4(\eta_3-\eta_1)}{(\eta_3-\eta_4)\tanh^2\left(\frac{\sqrt{(\eta_1-\eta_3)(\eta_2-\eta_4)}}{2}\sqrt{\frac{-F}{2}}(\mu-\mu_0)\right)-(\eta_3-\eta_1)}\exp^{\left[i\left(-\kappa t+\psi x+p\right)\right]}. \tag{86}$$

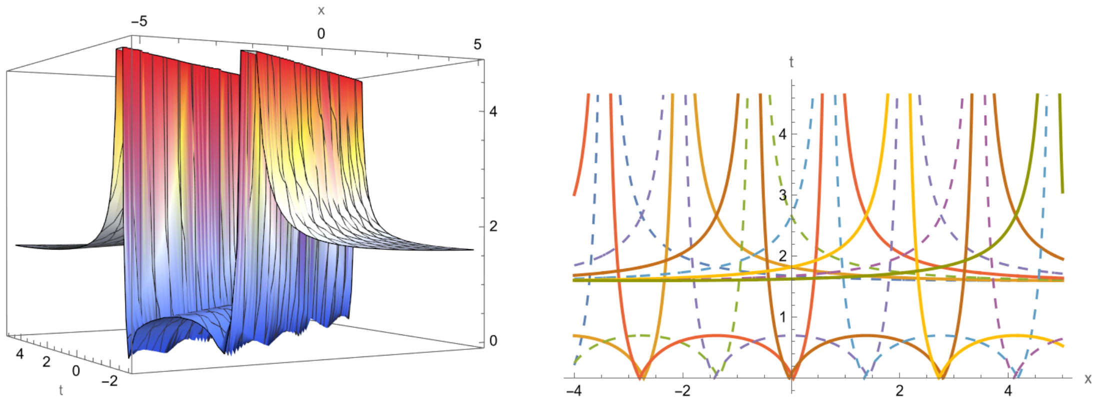


Figure 26: Equation (85) express the visual representation of $\varpi(x,t)$ when $\eta_1 = 1.5$, $\eta_2 = 0.7$, $\eta_3 = 1.6$, $\eta_4 = 2.7$, $\varsigma_1 = 1$, $\varsigma_2 = 2.3$, $\psi = 0.7$, $\mu_0 = 0$, $p = 0$, $\kappa = 0.5$.

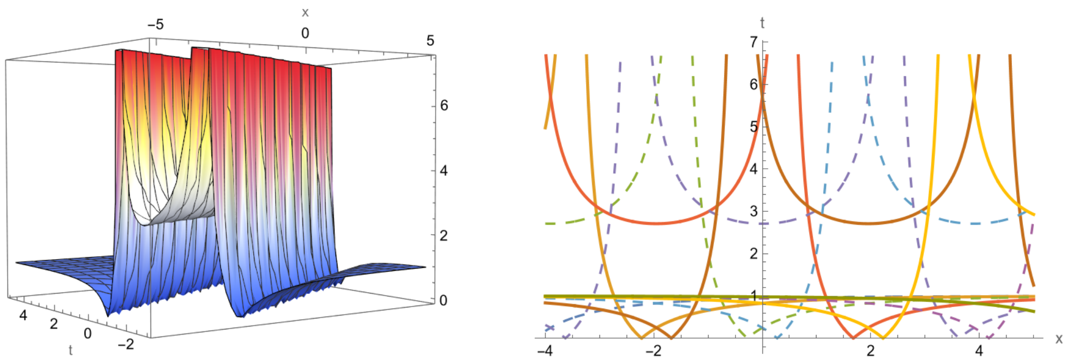


Figure 27: Equation (86) depicts the figure of $\varpi(x,t)$ when $\eta_1 = 1.53$, $\eta_2 = 0.73$, $\eta_3 = 1$, $\eta_4 = 2.71$, $\varsigma_1 = 1.01$, $\varsigma_2 = 2.03$, $\psi = 0.7$, $\mu_0 = 0$, $p = 0$, $\kappa = 0.5$.

## 5.2 Double periodic-I SW

By having the limit $\alpha \to 0$ in equation (44) and equation (45), then the function convert into

$$sn^2\left(\frac{\sqrt{(\eta_1-\eta_3)(\eta_2-\eta_4)}}{2}\sqrt{\frac{-F}{2}}(\mu-\mu_0),\alpha\right) \to \sin^2\left(\frac{\sqrt{(\eta_1-\eta_3)(\eta_2-\eta_4)}}{2}\sqrt{\frac{-F}{2}}(\mu-\mu_0)\right),$$

which display the SW solutions[15]:

$$\varpi(x,t)=\frac{\eta_3(\eta_1-\eta_2)\sin^2\left(\frac{\sqrt{(\eta_1-\eta_3)(\eta_2-\eta_4)}}{2}\sqrt{\frac{-F}{2}}(\mu-\mu_0)\right)-\eta_2(\eta_1-\eta_3)}{(\eta_1-\eta_2)\sin^2\left(\frac{\sqrt{(\eta_1-\eta_3)(\eta_2-\eta_4)}}{2}\sqrt{\frac{-F}{2}}(\mu-\mu_0)\right)-(\eta_1-\eta_3)}\exp^{\left[i\left(-\kappa t+\psi x+p\right)\right]}, \tag{87}$$

$$\varpi(x,t)=\frac{\eta_1(\eta_3-\eta_4)\sin^2\left(\frac{\sqrt{(\eta_1-\eta_3)(\eta_2-\eta_4)}}{2}\sqrt{\frac{-F}{2}}(\mu-\mu_0)\right)-\eta_4(\eta_3-\eta_1)}{(\eta_3-\eta_4)\sin^2\left(\frac{\sqrt{(\eta_1-\eta_3)(\eta_2-\eta_4)}}{2}\sqrt{\frac{-F}{2}}(\mu-\mu_0)\right)-(\eta_3-\eta_1)}\exp^{\left[i\left(-\kappa t+\psi x+p\right)\right]}. \tag{88}$$

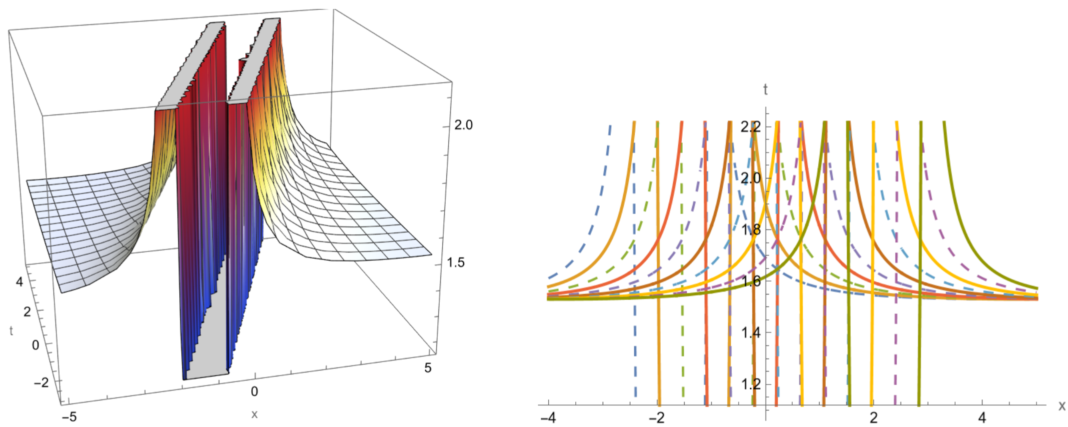


Figure 28: Equation (87) display the visual dynamics of $\varpi(x,t)$ when $\eta_1=1.53$, $\eta_2=0.73$, $\eta_3=1.4$, $\eta_4=2.41$, $\varsigma_1=1.01$, $\varsigma_2=2.03$, $\psi=0.7$, $\mu_0=0$, $p=0$, $\kappa=0.8$.

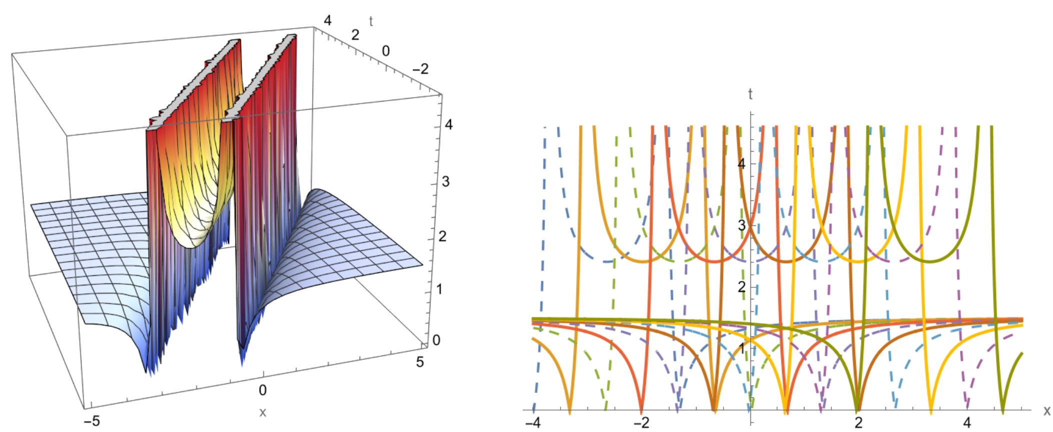


Figure 29: Equation (88) shows a representation of $\varpi(x,t)$ when $\eta_1=1.51$, $\eta_2=0.71$, $\eta_3=1.5$, $\eta_4=2.41$, $\varsigma_1=1.01$, $\varsigma_2=2.01$, $\phi=0.701$, $\mu_0=0$, $p=0$, $\kappa=0.7$.

### 5.3 Double hyperbolic-I SW

By having the limit $\alpha \to 1$ in equation (49), then the function transfer into

$$cn\left(\frac{\sqrt{\mp 2K\alpha_1(\vartheta-\xi)}}{2\alpha\alpha_1}\sqrt{\frac{-F}{2}}(\mu-\mu_0),\alpha\right) \to \sec h\left(\frac{\sqrt{\mp 2K\alpha_1(\vartheta-\xi)}}{2\alpha\alpha_1}\sqrt{\frac{-F}{2}}(\mu-\mu_0)\right),$$

which show the SW solution[15]:

$$\varpi(x,t)=\frac{P\sec h\left(\frac{\sqrt{\mp 2K\alpha_1(\vartheta-\xi)}}{2\alpha\alpha_1}\sqrt{\frac{-F}{2}}(\mu-\mu_0)\right)+Q}{R\sec h\left(\frac{\sqrt{\mp 2K\alpha_1(\vartheta-\xi)}}{2\alpha\alpha_1}\sqrt{\frac{-F}{2}}(\mu-\mu_0)\right)+S}\exp^{\left[i\left(-\kappa t+\psi x+p\right)\right]}. \tag{89}$$

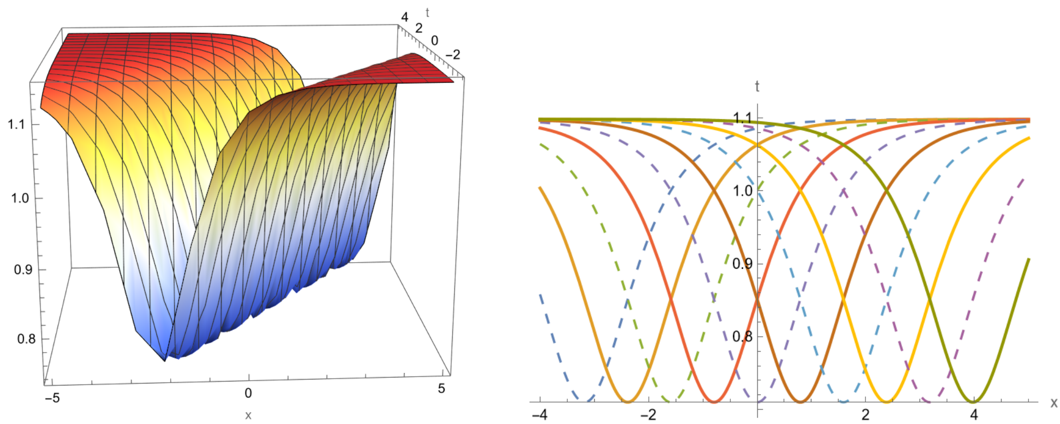


Figure 30: Equation (89) express the visual display of $\varpi(x,t)$ when $\vartheta = 1.51$, $\xi = 0.71$, $\sigma = 1.52$, $K = 2.31$, $\varsigma_1 = 1.06$, $\varsigma_2 = 2.08$, $\psi = 0.68$, $\mu_0 = 0$, $p = 0$, $\kappa = 0.65$.

### 5.4 Double periodic-II SW

By having the limit $\alpha \to 0$ in equation (49), then the function transfer into

$$cn\left(\frac{\sqrt{\mp 2K\alpha_1(\vartheta-\xi)}}{2\alpha\alpha_1}\sqrt{\frac{-F}{2}}(\mu-\mu_0),\alpha\right) \to \cos\left(\frac{\sqrt{\mp 2K\alpha_1(\vartheta-\xi)}}{2\alpha\alpha_1}\sqrt{\frac{-F}{2}}(\mu-\mu_0)\right),$$

which show the SW solution [15]:

$$\varpi(x,t)=\frac{P\cos\left(\frac{\sqrt{\mp 2K\alpha_1(\vartheta-\xi)}}{2\alpha\alpha_1}\sqrt{\frac{-F}{2}}(\mu-\mu_0)\right)+Q}{R\cos\left(\frac{\sqrt{\mp 2K\alpha_1(\vartheta-\xi)}}{2\alpha\alpha_1}\sqrt{\frac{-F}{2}}(\mu-\mu_0)\right)+S}\exp^{\left[i\left(-\kappa t+\psi x+p\right)\right]}. \tag{90}$$

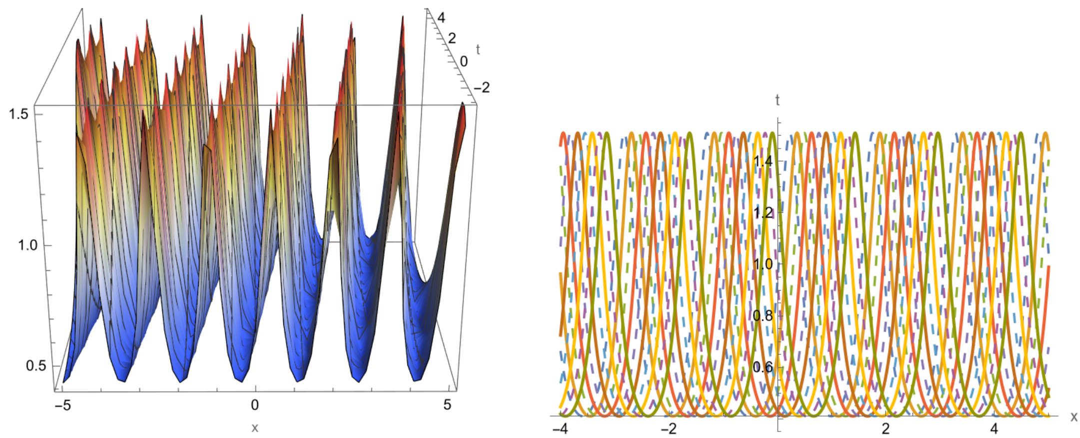


Figure 31: Equation (90) presents visual depiction of $\varpi(x,t)$ when $\vartheta = 1.51$, $\xi = 0.41$, $\sigma = 1.52$, $K = 0.31$, $\varsigma_1 = 1.1$, $\varsigma_2 = 2.18$, $\psi = 0.68$, $\mu_0 = 0$, $p = 0$, $\kappa = 1.25$.

## 5.5 Double hyperbolic-III SW

When having the limit $\alpha \to 1$ in equation (53), then the functions transform into

$$sn\left(\nu\sqrt{\frac{-F}{2}}(\mu-\mu_0),\alpha\right) \to \tanh\left(nu\sqrt{\frac{-F}{2}}(\mu-\mu_0)\right),$$

and

$$cn\left(\nu\sqrt{\frac{-F}{2}}(\mu-\mu_0),\alpha\right) \to \sec h\left(\nu\sqrt{\frac{-F}{2}}(\mu-\mu_0)\right),$$

which show the SW solution[15]:

$$\varpi(x,t) = \frac{R\tanh\left(\nu\sqrt{\frac{-F}{2}}(\mu-\mu_0)\right) + S\sec h\left(\nu\sqrt{\frac{-F}{2}}(\mu-\mu_0)\right)}{T\tanh\left(\nu\sqrt{\frac{-F}{2}}(\mu-\mu_0)\right) + U\sec h\left(\nu\sqrt{\frac{-F}{2}}(\mu-\mu_0)\right)} \exp^{\left[i\left(-\kappa t+\psi x+p\right)\right]}, \tag{91}$$

where $\nu = \dfrac{e_2\sqrt{(T^2+U^2)(\delta_1^2 T^2+U^2)}}{T^2+U^2}$.

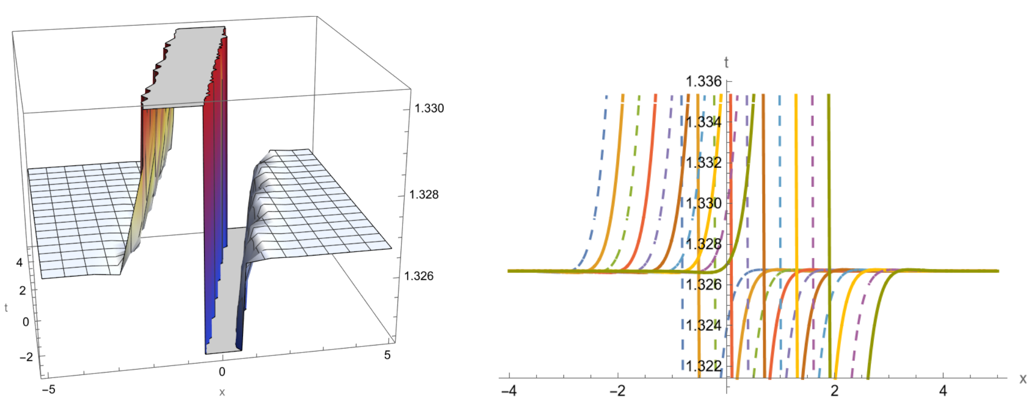


Figure 32: Equation (91) depicts visual display of $\varpi(x,t)$ when $d_1 = 1.51$, $d_2 = 2.7$, $e_1 = 0.41$, $e_2 = 1.6$, $\varsigma_1 = 1.1$, $\varsigma_2 = 2.18$, $\psi = 0.68$, $\mu_0 = 0$, $p = 0.001$, $\kappa = 0.9$.

### 5.6 Double periodic-III SW

When having the limit $\alpha \to 0$ in equation (53), then the functions transform into

$$sn\left(\nu\sqrt{\frac{-F}{2}}(\mu-\mu_0),\alpha\right) \to \sin\left(nu\sqrt{\frac{-F}{2}}(\mu-\mu_0)\right),$$

and

$$cn\left(\nu\sqrt{\frac{-F}{2}}(\mu-\mu_0),\alpha\right) \to \cos\left(\nu\sqrt{\frac{-F}{2}}(\mu-\mu_0)\right),$$

which show the SW solution[15]:

$$\varpi(x,t) = \frac{R\sin\left(\nu\sqrt{\frac{-F}{2}}(\mu-\mu_0)\right)+S\cos\left(\nu\sqrt{\frac{-F}{2}}(\mu-\mu_0)\right)}{T\sin\left(\nu\sqrt{\frac{-F}{2}}(\mu-\mu_0)\right)+U\cos\left(\nu\sqrt{\frac{-F}{2}}(\mu-\mu_0)\right)}\exp^{\left[i\left(-\kappa t+\psi x+p\right)\right]}, \tag{92}$$

where $\nu = \dfrac{e_2\sqrt{(T^2+U^2)(\alpha_1^2T^2+U^2)}}{T^2+U^2}$.

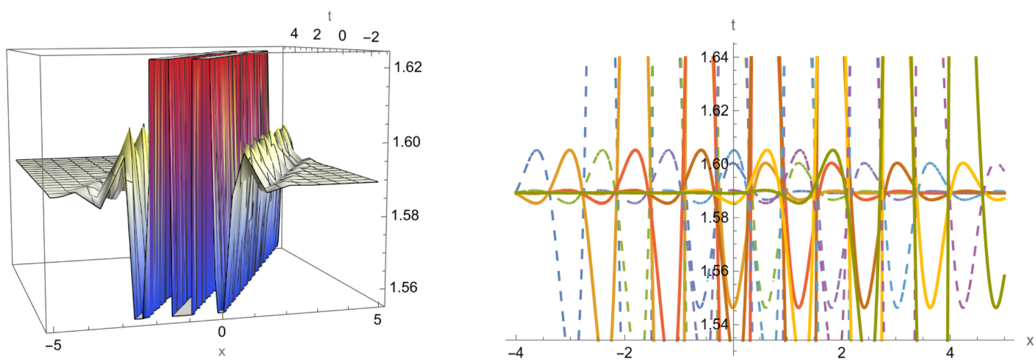


Figure 33: Equation (92) express a dynamical illustration of $\varpi(x,t)$ when $d_1 = 1.53$, $d_2 = 2.73$, $e_1 = 0.43$, $e_2 = 1.62$, $\varsigma_1 = 1.1$, $\varsigma_2 = 2.17$, $\psi = 0.67$, $\mu_0 = 0$, $p = 0$, $\kappa = 0.7$.

### 5.7 Double hyperbolic-IV SW

When containing the limit $\alpha \to 1$ in equation (80), then the function becomes

$$sn^2\left(\frac{\sqrt{\theta-\zeta}}{2}\sqrt{\frac{-F}{2}}(\mu-\mu_0),\alpha\right) \to \tanh^2\left(\frac{\sqrt{\theta-\zeta}}{2}\sqrt{\frac{-F}{2}}(\mu-\mu_0)\right),$$

which express the SW solution[15]:

$$\varpi(x,t) = \sqrt{\zeta+(\eta-\zeta)\tanh^2\left(\frac{\sqrt{\theta-\zeta}}{2}\sqrt{\frac{-F}{2}}(\mu-\mu_0)\right)}\exp^{\left[i\left(-\kappa t+\psi x+p\right)\right]}. \tag{93}$$

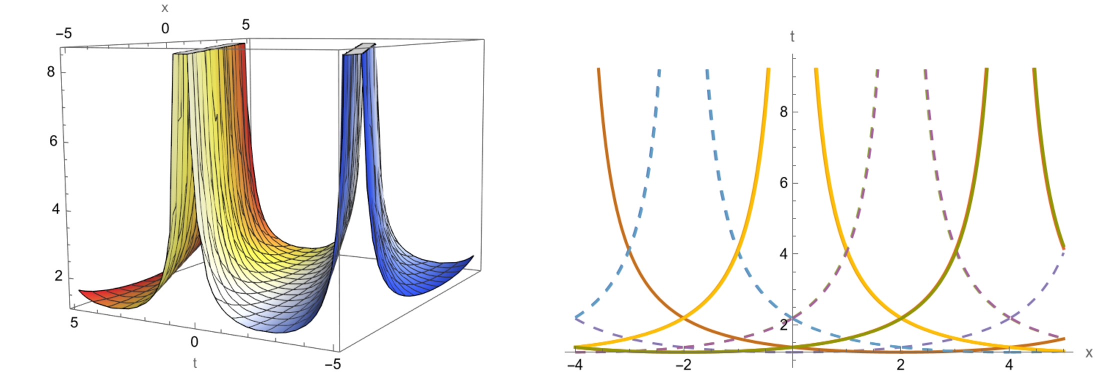


Figure 34: Equation (93) present a graph of $\varpi(x,t)$ when $\zeta = 1.52$, $\eta = 0.42$, $\theta = 1.52$, $\varsigma_1 = 1.1$, $\varsigma_2 = 2.13$, $\psi = 0.63$, $\mu_0 = 0$, $p = 0.003$, $\kappa = 0.5$.

### 5.8 Double periodic-IV SW

When containing the limit $\alpha \to 0$ in equation (80), then the function becomes

$$sn^2\left(\frac{\sqrt{\theta-\zeta}}{2}\sqrt{\frac{-F}{2}}(\mu-\mu_0),\alpha\right) \to \sin^2\left(\frac{\sqrt{\theta-\zeta}}{2}\sqrt{\frac{-F}{2}}(\mu-\mu_0)\right),$$

which express the SW solution[15]:

$$\varpi(x,t) = \sqrt{\zeta + (\eta-\zeta)\sin^2\left(\frac{\sqrt{\theta-\zeta}}{2}\sqrt{\frac{-F}{2}}(\mu-\mu_0)\right)}\exp^{\left[i\left(-\kappa t+\psi x+p\right)\right]}. \tag{94}$$

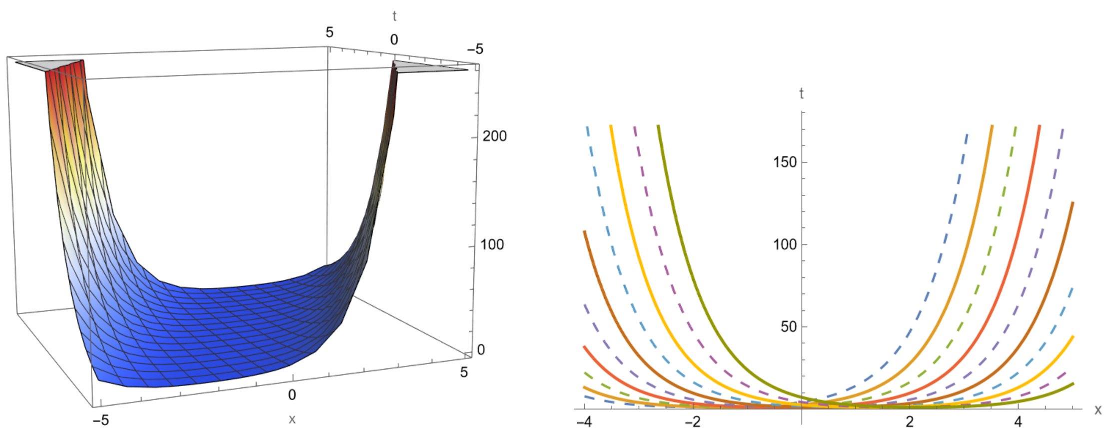


Figure 35: Equation (94) depicts a dynamics of $\varpi(x,t)$ when $\zeta = 1.5$, $\eta = 0.4$, $\theta = 1.52$, $\varsigma_1 = 1.09$, $\varsigma_2 = 2.1$, $\phi = 0.63$, $\mu_0 = 0$, $p = 0.003$, $\kappa = 0.8$.

### 5.9 Double hyperbolic-V SW

When containing the limit $\alpha \to 1$ in equation (81), then the function becomes

$$sn^2\left(\frac{\sqrt{\theta-\zeta}}{2}\sqrt{\frac{-F}{2}}(\mu-\mu_0),\alpha\right) \to \tanh^2\left(\frac{\sqrt{\theta-\zeta}}{2}\sqrt{\frac{-F}{2}}(\mu-\mu_0)\right),$$

and

$$cn^2\left(\frac{\sqrt{\theta-\zeta}}{2}\sqrt{\frac{-F}{2}}(\mu-\mu_0),\alpha\right) \to \sec h^2\left(\frac{\sqrt{\theta-\zeta}}{2}\sqrt{\frac{-F}{2}}(\mu-\mu_0)\right),$$

which express the SW solution[15]:

$$\varpi(x,t) = \sqrt{\frac{\theta-\eta\tanh^2\left(\frac{\sqrt{\theta-\zeta}}{2}\sqrt{\frac{-F}{2}}(\mu-\mu_0)\right)}{\sec h^2\left(\frac{\sqrt{\theta-\zeta}}{2}\sqrt{\frac{-F}{2}}(\mu-\mu_0)\right)}}\exp^{\left[i\left(-\kappa t+\psi x+p\right)\right]}. \tag{95}$$

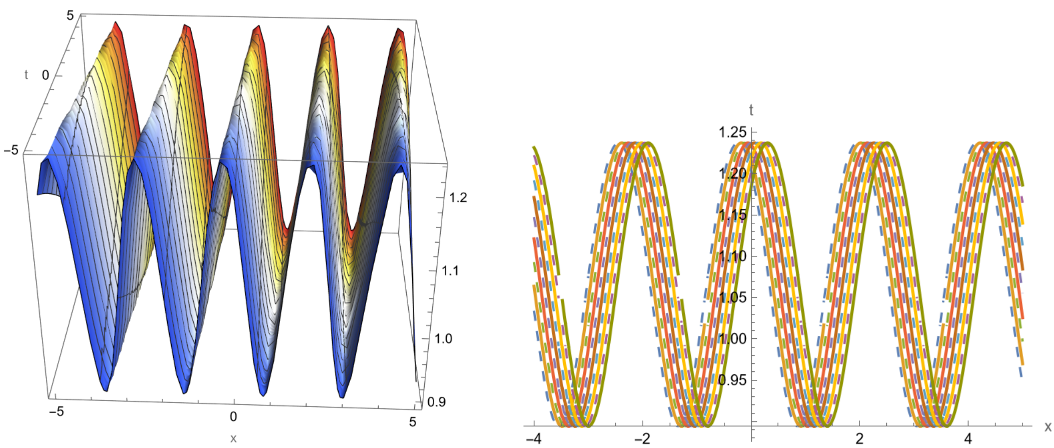


Figure 36: Equation (95) presents a graphical illustration of $\varpi(x,t)$ when $\zeta = 1.5$, $\eta = 0.8$, $\theta = 1.52$, $\varsigma_1 = 1.09$, $\varsigma_2 = 2.1$, $\psi = 0.63$, $\mu_0 = 0$, $p = 0.003$, $\kappa = 1.8$.

### 5.10 Double periodic-V SW

When containing the limit $\alpha \to 0$ in equation (81), then the function becomes

$$sn^2\left(\frac{\sqrt{\theta-\zeta}}{2}\sqrt{\frac{-F}{2}}(\mu-\mu_0),\alpha\right) \to \sin^2\left(\frac{\sqrt{\theta-\zeta}}{2}\sqrt{\frac{-F}{2}}(\mu-\mu_0)\right),$$

and

$$cn^2\left(\frac{\sqrt{\theta-\zeta}}{2}\sqrt{\frac{-F}{2}}(\mu-\mu_0),\alpha\right) \to \cos^2\left(\frac{\sqrt{\theta-\zeta}}{2}\sqrt{\frac{-F}{2}}(\mu-\mu_0)\right),$$

which express the SW solution[15]:

$$\varpi(x,t) = \sqrt{\frac{\theta - \eta \sin^2\left(\frac{\sqrt{\theta-\zeta}}{2}\sqrt{\frac{-F}{2}}(\mu-\mu_0)\right)}{\cos^2\left(\frac{\sqrt{\theta-\zeta}}{2}\sqrt{\frac{-F}{2}}(\mu-\mu_0)\right)}}\exp^{\left[i\left(-\kappa t+\psi x+p\right)\right]}. \tag{96}$$

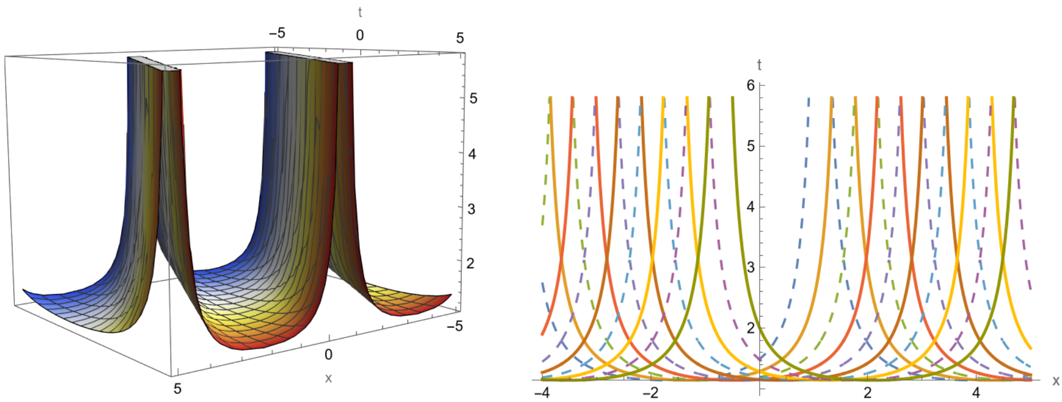


Figure 37: Equation (96) shows a graphical presentation of $\varpi(x,t)$ during the time period when $\zeta = 1.52$, $\eta = 0.81$, $\theta = 1.3$, $\varsigma_1 = 1.52$, $\varsigma_2 = 2.15$, $\psi = 0.61$, $\mu_0 = 0$, $p = 0.003$, $\kappa = 0.8$.

### 5.11 Bright SW

Upon having the limit $\alpha \to 1$ in equation (84), then the function convert into

$$cn\left((\pi^2+g\pi+h)^{\frac{1}{4}}\sqrt{\frac{-F}{2}}(\mu-\mu_0),\alpha\right) \to \sec h\left((\pi^2+g\pi+h)^{\frac{1}{4}}\sqrt{\frac{-F}{2}}(\mu-\mu_0)\right),$$

that are present the SW solution[15]:

$$\varpi(x,t) = \sqrt{\pi - \sqrt{\pi^2+g\pi+h} + \frac{2\sqrt{\pi^2+g\pi+h}}{1+\sec h\left((\pi^2+g\pi+h)^{\frac{1}{4}}\sqrt{\frac{-F}{2}}(\mu-\mu_0)\right)}}\exp^{\left[i\left(-\kappa t+\psi x+p\right)\right]}. \tag{97}$$

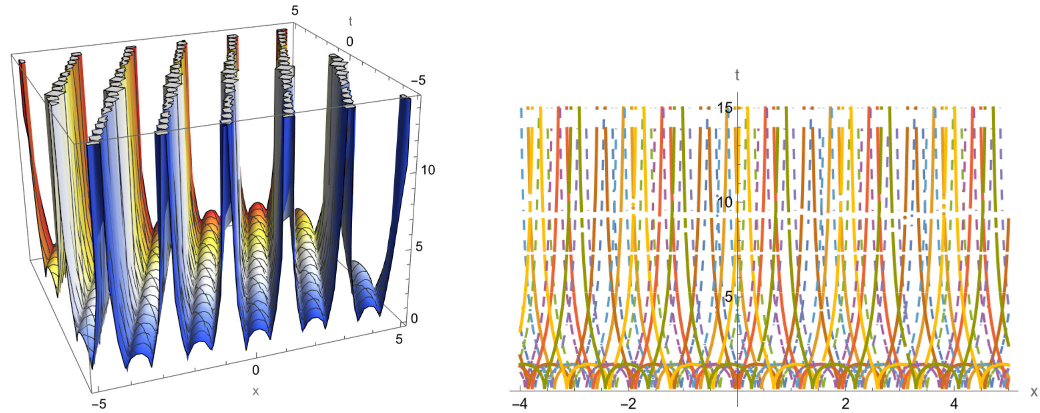


Figure 38: Equation (97) shows the graph of $\varpi(x,t)$ when $\phi = 1.55$, $g = 0.31$, $h = 0.72$, $\varsigma_1 = 1.09$, $\varsigma_2 = 2.15$, $\psi = 0.64$, $\mu_0 = 0$, $p = 0.003$, $\kappa = 0.85$.

### 5.12 Periodic SW

Upon having the limit $\alpha \to 0$ in equation (84), then the function convert into

$$cn\left((\pi^2+g\pi+h)^{\frac{1}{4}}\sqrt{\frac{-F}{2}}(\mu-\mu_0),\alpha\right) \to \cos\left((\pi^2+g\pi+h)^{\frac{1}{4}}\sqrt{\frac{-F}{2}}(\mu-\mu_0)\right),$$

that are present the SW solution[15]:

$$\varpi(x,t) = \sqrt{\pi - \sqrt{\pi^2+g\pi+h} + \frac{2\sqrt{\pi^2+g\pi+h}}{1+\cos\left((\pi^2+g\pi+h)^{\frac{1}{4}}\sqrt{\frac{-F}{2}}(\mu-\mu_0)\right)}}\,\exp^{\left[i\left(-\kappa t+\psi x+p\right)\right]}. \tag{98}$$

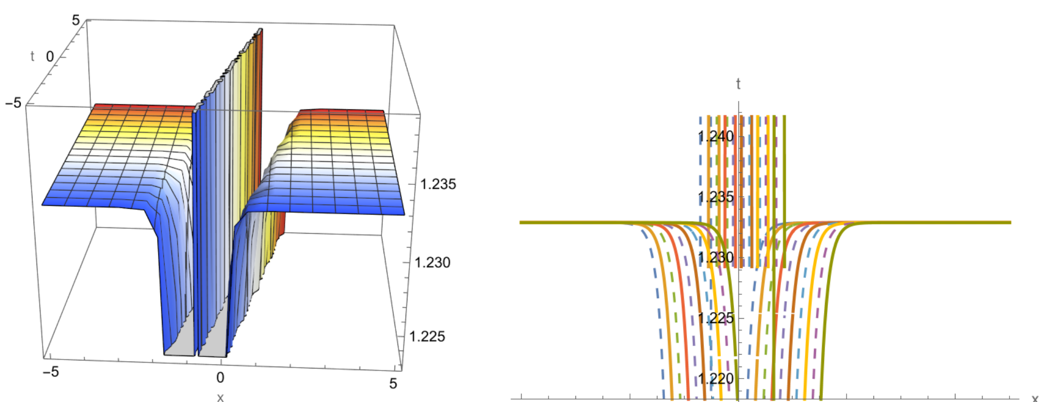


Figure 39: Equation (98) express the plot of $\varpi(x,t)$ when $\phi = 1.55$, $g = 0.31$, $h = 0.72$, $\varsigma_1 = 1.09$, $\varsigma_2 = 2.15$, $\psi = 0.64$, $\mu_0 = 0$, $p = 0.003$, $\kappa = 0.85$.

## 6 Results and Discussion

In this section, we will go through our findings. Liu et al. [30] investigated the TONLSE utilizing the Hirotas bilinear approach to provide one and two-solution solutions. Özkan et al. [20] investigated the TONLSE, which describes wave pulse transmission in less than one trillionth of a second. They utilized the extended modified technique and the Lie symmetry groups approach to obtain exact solutions. Wang et al. [34] examined the dark soliton control for the TONLSE using different dispersion and nonlinearity. Rizvi et al. [26] investigated the characteristics and existence of propagating solitary waves in a fiber optic medium using the TONLSE and an optical metamaterial with quadratic-cubic nonlinearity. Chowdury et al. [13] investigated the Hirota equation, which allows for breather-to-soliton conversion for particular eigenvalues of the solution. Yongsheng and Jingsong [31] addressed the Hirota equation and used the Darboux transformation to determine the 1-soliton, 2-soliton, and breather solutions.

Our derived results are now thoroughly examined. We investigate the dynamic characteristics and find the exact answers using the CDSPM and also convert our JEF into SW soltions. The global phase depictions illustrate the efficiency of CDS not only in getting different sorts of solutions but also in carrying out qualitative analysis by demonstrating that the topological aspects of the solution change as the parameters change. We can find the variety of solutions that are, equations (24), and (73) represent the periodic solutions. Equations (31), (32), (40), (71) and (72), express a SW solutions. Equations (27), (36) and (37) show a rational solutions. While (44) and (45) express the JEF double periodic solutions but when $\alpha \to 1$ and $\alpha \to 0$, it change into double hyperbolic-I SW in (85) and (86) and double periodic-I SW in (87) and (88). Equation (49) demonstrate the JEF double periodic solutions but by having the limit $\alpha \to 1$ and $\alpha \to 0$ it change into double hyperbolic-II SW in (89) and double periodic-II SW in (90). Equation (53) represent the JEF double periodic solution but when we take limit $\alpha \to 1$ and $\alpha \to 0$ it transform into the double hyperbolic-III in (91) and double periodic-III in (92). Equation (80) present a JEF solution but in (93), it transfer into double hyperbolic-IV SW when $\alpha \to 1$ and in (94), it transform into double periodic-IV SW when $\alpha \to 0$. Equation (81) also show JEF solution but in (95) and (96), it convert into double hyperbolic-V SW and double periodic-V SW and when $\alpha \to 1$ and $\alpha \to 0$. Equation (84) also present a JEF solution but when we approach $\alpha \to 1$ and $\alpha \to 0$ then, it degenerate into bright SW and periodic SW. The dynamical behaviour of these solutions are also display.

## 7 Conclusions

This paper analyses the TONLSE using qualitative analysis to obtain phase illustrations and equilibrium points. Additionally, we utilize bifurcation methods to prove the existence of periodic and soliton solutions. We can produce various kinds of solutions, including periodic, SW, rational, elliptic function and elliptic function double periodic solutions and also convert JEF and JEF double periodic solutions into SW solutions. Our understanding of the general behaviour of polarisation modes in optical fibres is improved by the findings of this study. Additionally, the findings might be put to use in a variety of industries, such as laser drilling, intelligent water injection, and pipeline network optimisation for oil and gas. The development of effective and affordable approaches in these areas may greatly benefit from these applications.

**Acknowledgement** The authors are very grateful to the referees for their kind comments and valuable suggestions that helped improve this work.

**Conflicts of Interest** The authors declare no conflict of interest.

## References

[1] H. Ahmad, T. A. Khan, P. S. Stanimirovic, W. Shatanawi & T. Botmart (2022). New approach on conventional solutions to nonlinear partial differential equations describing physical phenomena. *Results in Physics*, *41*, Article ID: 105936. https://doi.org/10.1016/j.rinp.2022.105936.

[2] H. Ahmad, A. R. Seadawy & T. A. Khan (2020). Numerical solution of Korteweg-de Vries-Burgers equation by the modified variational iteration algorithm-II arising in shallow water waves. *Physica Scripta*, *95*(4), Article ID: 045210. https://doi.org/10.1088/1402-4896/ab6070.

[3] I. Ali, S. T. R. Rizvi, S. O. Abbas & Q. Zhou (2019). Optical solitons for modulated compressional dispersive alfven and heisenberg ferromagnetic spin chains. *Results in Physics*, *15*, Article ID: 102714. https://doi.org/10.1016/j.rinp.2019.102714.

[4] M. R. Ali, M. A. Khattab & S. M. Mabrouk (2023). Optical soliton solutions for the integrable lakshmanan-porsezian-daniel equation via the inverse scattering transformation method with applications. *Optik*, *272*, Article ID: 17056. https://doi.org/10.1016/j.ijleo.2022.170256.

[5] F. S. Alshammari, M. F. Hoque & M. Nadeem (2023). Bifurcation analysis and bounded optical soliton solutions of the Biswas-Arshed model. *Computer Modeling in Engineering and Sciences*, *135*(3), 2197–2217. https://doi.org/10.32604/cmes.2023.022301.

[6] M. I. Asjad, W. A. Faridi, S. E. Alhazmi & A. Hussanan (2023). The modulation instability analysis and generalized fractional propagating patterns of the Peyrard-Bishop DNA dynamical equation. *Optical and Quantum Electronics*, *55*(232), 1–34. https://doi.org/10.1007/s11082-022-04477-y.

[7] N. Aziz, A. R. Seadawy, K. Ali, M. Sohail & S. T. R. Rizvi (2022). The nonlinear Schrödinger equation with polynomial law nonlinearity: localized chirped optical and solitary wave solutions. *Optical and Quantum Electronics*, *54*(7), Article ID: 458. https://doi.org/10.1007/s11082-022-03831-4.

[8] T. Batool, A. R. Seadawy, S. T. R. Rizvi & K. Ali (2022). Homoclinic breather, $m$-shaped rational, multiwaves and their interactional solutions for fractional quadratic-cubic nonlinear Schrödinger equation. *Optical and Quantum Electronics*, *54*(12), Article ID: 844. https://doi.org/10.1007/s11082-022-04280-9.

[9] L. Cheng-Shi (2007). Classification of all single travelling wave solutions to Calogero-Degasperis-Focas equation. *Communications in Theoretical Physics*, *48*(4), Article ID: 601. https://doi.org/10.1088/0253-6102/48/4/004.

[10] L. Cheng-Shi (2008). Representations and classification of traveling wave solutions to Sinh-Gördon equation. *Communications in Theoretical Physics*, *49*(1), 153–158. https://doi.org/10.1088/0253-6102/49/1/33.

[11] L. Cheng-Shi (2008). Solution of ODE $u'' + p(u)(u')^2 + q(u) = 0$ and applications to classifications of all single travelling wave solutions to some nonlinear mathematical physics equations. *Communications in Theoretical Physics*, *49*(2), 291–296. https://ctp.itp.ac.cn/EN/Y2008/V49/I02/291.

[12] L. Cheng-Shi (2010). Applications of complete discrimination system for polynomial for classifications of traveling wave solutions to nonlinear differential equations. *Computer Physics Communications*, *181*(2), 317–24. https://doi.org/10.1016/j.cpc.2009.10.006.

[13] A. Chowdury, A. Ankiewicz & N. Akhmediev (2015). Moving breathers and breather-to-soliton conversions for the Hirota equation. *Proceedings of the Royal Society A: Mathematical, Physical and Engineering Sciences*, *471*(2810), Article ID: 20150130. https://doi.org/10.1098/rspa.2015.0130.

[14] M. Eslami, B. F. Vajargah & M. Mirzazadeh (2014). Exact solutions of modified Zakharov-Kuznetsov equation by the homogeneous balance method. *Ain Shams Engineering Journal*, *5*(1), 221–225. https://doi.org/10.1016/j.asej.2013.06.005.

[15] A. Filiz, M. Ekici, A. Sonmezoglu et al. (2014). $F$-expansion method and new exact solutions of the Schrödinger-KdV equation. *The Scientific World Journal*, *2014*, Article ID: 3928877. https://doi.org/10.1155/2014/534063.

[16] M. M. Hossain, A. Abdeljabbar, H.-O. Roshid, M. M. Roshid & A. N. Sheikh (2022). Abundant bounded and unbounded solitary, periodic, rogue-type wave solutions and analysis of parametric effect on the solutions to nonlinear Klein-Gordon model. *Complexity*, *2022*, Article ID: 8771583, 19 pages. https://doi.org/10.1155/2022/8771583.

[17] Y. Kai, S. Chen, B. Zheng, K. Zhang, N. Yang & W. Xu (2020). Qualitative and quantitative analysis of nonlinear dynamics by the complete discrimination system for polynomial method. *Chaos, Solitons and Fractals*, *141*(62), Article ID: 110314. https://doi.org/10.1016/j.chaos.2020.110314.

[18] X. Li, Z. Zhang, Q. Zhao & C. Li (2022). Darboux transformation of two novel two-component generalized complex short pulse equations. *Reports on Mathematical Physics*, *90*(2), 157–184. https://doi.org/10.1016/S0034-4877(22)00063-5.

[19] S. Z. Majid, W. A. Faridi, M. I. Asjad, M. Abd El-Rahman & S. M. Eldin (2023). Explicit soliton structure formation for the riemann wave equation and a sensitive demonstration. *Fractal and Fractional*, *7*(2), Article ID: 102. https://doi.org/10.3390/fractalfract7020102.

[20] Y. S. Özkan, E. Yaşar & A. R. Seadawy (2020). A third-order nonlinear Schrödinger equation: the exact solutions, group-invariant solutions and conservation laws. *Journal of Taibah University for Science*, *14*(1), 585–597. https://doi.org/10.1080/16583655.2020.1760513.

[21] Z. Rahman, M. Z. Ali & H.-O. Roshid (2021). Closed form soliton solutions of three nonlinear fractional models through proposed improved Kudryashov method. *Chinese Physics B*, *30*(5), Article ID: 050202. https://doi.org/10.1088/1674-1056/abd165.

[22] H. Rezazadeh (2018). New solitons solutions of the complex Ginzburg-Landau equation with Kerr law nonlinearity. *Optik*, *167*, 218–227. https://doi.org/10.1016/j.ijleo.2018.04.026.

[23] S. T. R. Rizvi, A. R. Seadawy, M. Hanif, M. Younis, K. Ali & A. Althobaiti (2022). Investigation of chirp-free dromions to higher order nonlinear Schrödinger equation with non kerr terms. *International Journal of Modern Physics B*, *36*(5), Article ID: 2250043. https://doi.org/10.1142/S0217979222500436.

[24] S. T. R. Rizvi, A. R. Seadawy, S. Ahmed, M. Younis & K. Ali (2021). Study of multiple lump and rogue waves to the generalized unstable space time fractional nonlinear Schrödinger equation. *Chaos, Solitons and Fractals*, *151*, Article ID: 111251. https://doi.org/10.1016/j.chaos.2021.111251.

[25] S. T. R. Rizvi, A. R. Seadawy, N. Farah & S. Ahmad (2022). Application of Hirota operators for controlling soliton interactions for Bose-Einstien condensate and quintic derivative nonlinear Schrödinger equation. *Chaos, Solitons & Fractals*, *159*(35), Article ID: 112128. https://doi.org/10.1016/j.chaos.2022.112128.

[26] S. T. R. Rizvi, A. R. Seadawy, S. Shabbir, S. Khizar & B. Mustafa (2023). Discussion on localized pulses for third-order nonlinear Schrödinger equation and negative index material with quadratic cubic nonlinearity. *International Journal of Modern Physics B*, *1*, Article ID: 2450065. https://doi.org/10.1142/S0217979224500656.

[27] A. R. Seadawy & N. Cheemaa (2020). Some new families of spiky solitary waves of one-dimensional higher-order K-dV equation with power law nonlinearity in plasma physics. *Indian Journal Physics*, *95*(1), 117–126. https://doi.org/10.1007/s12648-019-01442-6.

[28] A. R. Seadawy, D. Kumar & A. K. Chakrabarty (2018). Dispersive optical soliton solutions for the hyperbolic and cubic-quintic nonlinear Schrödinger equations via the extended sinh-Gordon equation expansion method. *The European Physical Journal Plus*, *133*(182), 1–12. https://doi.org/10.1140/epjp/i2018-12027-9.

[29] A. R. Seadawy, S. T. R. Rizvi, S. Ahmad, M. Younis & D. Baleanu (2021). Lump, lump-one stripe, multiwave and breather solutions for the Hunter-Saxton equation. *Open Physics*, *19*(1), 1–10. https://doi.org/10.1515/phys-2020-0224.

[30] K. Shah, A. R. Seadawy & M. Arfan (2020). Evaluation of one dimensional fuzzy fractional partial differential equations. *Alexandria Engineering Journal*, *59*(5), 3347–3353. https://doi.org/10.1016/j.aej.2020.05.003.

[31] Y. Tao & J. He (2012). Multisolitons, breathers, and rogue waves for the hirota equation generated by the Darboux transformation. *Physical Review E*, *85*(2), Article ID: 026601. https://doi.org/10.1103/physreve.85.026601.

[32] M. S. Ullah, M. Z. Ali, H.-O. Roshid & M. F. Hoque (2021). Collision phenomena among lump, periodic and stripe soliton solutions to a (2+1)-dimensional Bemjanim-Bona-Mahony-Burgers. *The European Physical Journal Plus*, *136*(370), 1–9. https://doi.org/10.1140/epjp/s13360-021-01343-w.

[33] M. S. Ullah, D. Baleanu, M. Z. Ali & H.-O. Roshid (2023). Novel dynamics of the Zoomeron model via different analytical methods. *Chaos, Solitons and Fractals*, *174*, Article ID: 653749. https://doi.org/10.1016/j.chaos.2023.113856.

[34] C. Wang, Z. Nie, W. Xie, J. Gao, Q. Zhou & W. Liu (2019). Dark soliton control based on dispersion and nonlinearity for third-order nonlinear Schrödinger equation. *Optik*, *184*(3), 370–376. https://doi.org/10.1016/j.ijleo.2019.04.020.

[35] J. Wang, K. Shehzad, A. R. Seadawy, M. Arshad & F. Asmat (2023). Dynamic study of multi-peak solitons and other wave solutions of new coupled KdV and new coupled zZakharov-Kuznetsov systems with their stability. *Journal of Taibah University for Science*, *17*(1), Article ID: 2163872. https://doi.org/10.1080/16583655.2022.2163872.

[36] U. Younas, A. R. Seadawy, M. Younis & S. T. R. Rizvi (2020). Optical solitons and closed form solutions to (3+1)-dimensional resonant Schrödinger equation. *International Journal of Modern Physics B*, *34*(30), Article ID: 2050291 16 pages. https://doi.org/10.1142/S0217979220502914.